



SO₂ solubility and degassing behavior in silicate melts

Julien Boulliung, Bernard J. Wood

Department of Earth Sciences, University of Oxford, South Parks Road, Oxford OX1 3AN, United-Kingdom

ARTICLE INFO

Article history:

Received 1 December 2021

Accepted 25 August 2022

Available online 30 August 2022

Associate editor: Bernard Charlier

Keywords:

Sulfate solubility

Sulfate capacity

Silicate melts

SO₂ degassing

ABSTRACT

We have determined the S contents of 14 different silicate melts equilibrated with Air/SO₂ mixtures at 1 atm pressure and temperatures of 1473–1773 K in 50 K intervals. Under these oxidizing conditions sulfur dissolves in the melts predominantly as sulfate (S⁶⁺ or SO₄^{2−}). The sulfur contents of the quenched products were determined by EPMA (Electron Probe Micro-Analysis) and by SIMS (Secondary Ion-Mass Spectrometry) with the latter being employed for low sulfur contents (i.e., ≤60 ppm). Equilibrium S contents were found to increase strongly with decreasing temperature and with some compositional parameters, especially CaO content. The data were used to calculate the sulfate capacity (log C_{S6+}), for each melt composition at each temperature. Sulfate capacity is related to the equilibrium constant for sulfur dissolution and is defined as follows in terms of SO₄^{2−} concentration and fugacities of oxygen and sulfur:

$$\log C_{S6+} = \log SO_{4melt} (wt. \%) - \frac{1}{2} \log f_{S_2} - \frac{3}{2} \log f_{O_2}$$

By determining log C_{S6+} at different Air/SO₂ ratios we showed that log C_{S6+} is independent of sulfur content and hence that Henry's Law is obeyed in the experimental composition and temperature range. We used stepwise linear regression to fit sulfate capacity to an equation incorporating compositional and temperature terms. Parameters which did not pass the F-test at the 95% confidence level were excluded. This approach led to the following fit equation:

$$\log C_{S6+} = -12.659 + (3692X_{CaO} - 7592X_{SiO_2} - 13736X_{TiO_2} + 3762X_{AlO_{1.5}} + 34483)/T$$

The standard error of the fit is 0.154 and R² is 0.985.

The data were used to simulate scenarios for SO₂-degassing from ascending silicate melts of basaltic and andesitic compositions. The important observations are that SO₂ partitions strongly into an H₂O-rich fluid phase and that most S is lost at relatively high pressures in the crust. So, for example we estimate that ≥85% of the initial S should be lost before the ascending magma reaches 100 MPa pressure.

© 2022 The Author(s). Published by Elsevier Ltd. This is an open access article under the CC BY license (<http://creativecommons.org/licenses/by/4.0/>).

1. Introduction

Knowledge of the solubility¹ of sulfur (S) in silicate melts is fundamental to an understanding of a number of igneous processes, including volcanic degassing, the formation of magmatic ore deposits and planetary differentiation (Jugo et al., 2005; Aiuppa et al., 2007, 2010; Edmonds et al., 2010; Botcharnikov et al., 2011; Simon and Ripley, 2011; Webster and Botcharnikov, 2011; Namur et al., 2016; Li et al., 2019). Several oxidation states of sulfur occur in natural environments and these exert controls over the distribution of sulfur between Earth's different geochemical reservoirs (mantle, core, crust, atmosphere, oceans). In magmatic systems sulfur is predominantly present either as sulfide (S^{2−}) or as sulfate (S⁶⁺ as

SO₄^{2−}) (Fincham and Richardson, 1954). Experimentally it has been found that sulfide dominates at oxygen fugacities below the Fayalite-Magnetite-Quartz (FMQ) buffer while sulfate is more stable under more oxidizing conditions (Fincham and Richardson, 1954; Carroll and Rutherford, 1985, 1987; Luhr, 1990; O'Neill and Mavrogenes 2002; Jugo et al., 2005; Morizet et al., 2017; Nash et al., 2019). Both sulfide and sulfate can, however, be present in oxidized magmatic rocks (e.g., Wallace and Carmichael, 1994; Wilke et al., 2008; Métrich et al., 2009; Jugo, 2009; Jugo et al., 2010; Parat et al., 2011; Grondahl and Zajacz, 2017; Chang and Audétat, 2018; Chen et al., 2020) with sometimes S predominantly as sulfate (e.g., Métrich and Clocchiatti, 1996; Gennaro, 2017; Morizet et al., 2017). Although the solubility of sulfide (S^{2−}) in silicate melts is well constrained (e.g., Namur et al., 2016), only a few data are available for sulfates even though sulfate-bearing minerals (e.g., apatite, nosean, haüyne) and sulfate minerals such as anhydrite (CaSO₄) are very well-known (Lindgren and Ransome, 1906; Brauns, 1914; Luhr et al., 1984). The presence of S as anhydrite and sulfide in magmatic rocks, in addition to the presence of SO₂ in volcanic gas,

E-mail addresses: julien.boulliung@earth.ox.ac.uk (J. Boulliung), bernie.wood@earth.ox.ac.uk (B.J. Wood)

¹ The solubility of sulfur is defined in this study as the sulfur concentration in the melt in equilibrium with a gas mixture of fixed composition at a given temperature and pressure.

indicates that there is significant S loss during magmatic degassing processes (Masotta and Keppler, 2015) leading, in some cases to changes in the oxidation state of Fe (Brounce et al., 2017). The behavior of SO₂ and sulfate in silicate melts needs, therefore, to be better understood in order to constrain magmatic degassing processes in oxidizing magmatic systems (e.g., arc magmatic systems).

Fincham and Richardson (1954) made a systematic experimental study of sulfur behavior in silicate melts. Under oxidizing conditions they observed a positive correlation between the logarithm of the S concentration and fO_2 indicating sulfur dissolution according to the reaction:



The equilibrium constant for reaction (1) is:

$$\log K = \log \frac{aSO_{4\text{melt}}^{2-}}{fS_2^{1/2} \cdot fO_2^{3/2} \cdot aO_{\text{melt}}^{2-}} \quad (2)$$

with $aSO_{4\text{melt}}^{2-}$ and aO_{melt}^{2-} corresponding to the activities of SO_4^{2-} and O^{2-} in the melt respectively and fO_2 , fS_2 being fugacities relative to standard states of pure gases at 1 bar and the temperature of interest. From Eq. (2), replacing sulfate activity $aSO_{4\text{melt}}^{2-}$ by concentration $[SO_{4\text{melt}}^{2-}]$ the sulfate capacity (C_{S6+}) is defined as follows:

$$\log C_{S6+} = \log SO_{4\text{melt}}^{2-} (\text{wt.}\%) - \frac{1}{2} \log fS_2 - \frac{3}{2} \log fO_2 \quad (3)$$

From Eqs. (2) and (3), the equilibrium constant K is related to the sulfate capacity as follows:

$$\log K + \log (aO_{\text{melt}}^{2-}) = \log C_{S6+} \quad (4)$$

The sulfate capacity thus combines the equilibrium constant for reaction (1) with the O^{2-} activity and is anticipated to be composition, temperature and pressure-dependent.

Tsujimura and Kitakaze (2005) performed experiments on sulfur solubility in silicate melts at 1523 K and 100 MPa and observed high sulfur content for FeO-free melts with a positive correlation between S concentration and CaO content. This correlation was attributed to the presence of sulfate in the melt, but as the fO_2 in these experiments was not well controlled, it is difficult to attribute this observation to sulfate presence alone. However, in the last twenty years, a number of studies have focused on sulfur concentration at anhydrite saturation (SCAS) and on development of models to predict S contents at SCAS (e.g., Moretti and Ottonello, 2005; Jugo et al., 2005, 2010; Jugo, 2009; Baker and Moretti, 2011; Masotta and Keppler, 2015; Zajacz and Tsay, 2019; Xu and Li, 2021). The experimental measurements of sulfur concentration at anhydrite saturation (SCAS) in silicate melts cover a temperature range from 1023 to 1598 K, pressures from 30 to 5000 MPa and for melt compositions from rhyolite to basalt (Carroll and Rutherford, 1987; Luhr, 1990; Clément et al., 2004; Costa et al., 2004; Jugo et al., 2005; Beermann et al., 2011; Zajacz et al., 2012; Huang and Keppler, 2015; Masotta and Keppler, 2015; Chowdhury and Dasgupta, 2019; Zajacz and Tsay, 2019; Xu and Li, 2021). Taken together the data show a negligible effect of pressure on SCAS but an increase of SCAS with increasing temperature and CaO contents of the silicate melts. It is important to note, however, that although these data on sulfate saturation are important to the understanding of sulfur behavior in oxidized magmas they have no obvious connection to the conditions under which SO₂ would be degassed from such melts. It was therefore the principal aim of our study to address the issue of SO₂ solubility and its dependence on composition and physical conditions.

In order to better understand the behavior of sulfur in oxidizing magmatic environments we followed the approach of Fincham and Richardson (1954) and determined the dependence of sulfate capacity on temperature and melt composition by performing experiments in an atmosphere-controlled furnace at high temperatures (from 1473 to 1773 K) using 14 different (mainly natural) melt compositions. Oxidizing redox conditions (i.e., $fO_2 > FMQ+4$) were imposed in order to incorporate S predominantly as sulfate in the silicate melts. The data obtained were used to develop an equation for the sulfate capacity of silicate melts as functions of their composition and the temperature. From this equation we developed a model to estimate the depths at which sulfur (dissolved as sulfate) will be degassed from the melts as SO₂.

2. Experimental and analytical methods

2.1. Starting materials

Previous work suggested a positive correlation between the Ca content of the melt and the sulfate concentration (e.g., Katsura and Nagashima, 1974; Luhr, 1990). In order to determine the effect of melt composition on sulfate capacity, fourteen synthetic and natural compositions with various CaO contents (i.e., from 1.0 to 22.3 wt%) were selected to represent a broad range of terrestrial and lunar igneous rocks (Table 1). A natural Icelandic Basalt (NIB) corresponded to a crushed and powdered natural basalt from Reykjanes Ridge (Iceland) (Norris and Wood, 2017; Thomas and Wood, 2021) while a powdered nepheline basanite UT-70489 (Adam, 1990; SiO₂ = 43.6 ± 0.1%) was supplied by Dr. J. Adam. Two other basaltic compositions, a lunar basalt (modeled from Apollo 11 basalt analyses; Hubbard and Gast, 1971) with 41.7 ± 0.2 wt% SiO₂ and one trachy-basalt (T-Basalt) from Taracsák et al. (2021) with higher SiO₂ content (i.e., 47.0 ± 0.1 wt%) were studied in order to determine the effects of low to moderate SiO₂ contents. Three iron-free CMAS compositions were also synthesized in order to constrain any potential iron effect on S solubility: CMAS1, a diopside-anorthite-forsterite mixture (i.e., Di₄₈An₄₇Fo₅) close to one eutectic in the system CaO–MgO–Al₂O₃–SiO₂ at 1 bar (Osborn and Tait, 1952); CMAS2 a mixture in a similar system (i.e., An₅₀Di₂₈Fo₂₂) but close to a 1.5 GPa eutectic (Presnall et al., 1978; Thomas and Wood, 2021); and CMAS3 an anorthite-diopside-enstatite mixture (En₁₇An₄₃Di₄₀) close to a second eutectic at 1573 K and 1 bar in the CaO–MgO–Al₂O₃–SiO₂ system (Hytönen and Schairer, 1961). The composition SL, corresponds to a synthetic composition representing a realistic planetary mantle composition with low liquidus temperature (i.e., ~1573 K; Sossi et al., 2019). Tephriphonolite (T-Phonolite) and nephelinite compositions were synthesized following analyses of Ridley (1970) and Webb and Dingwell (1990). Three different andesites were used, a basaltic-andesite “B-A”, with a high MgO content (i.e., 9.4 ± 0.2 wt%) (Wood and Turner, 2009), an “Andesite” corresponding to a sub-alkaline andesite with a high SiO₂ content (61.1 ± 0.1 wt%) and an andesite “Andac” close to the dacite classification (SiO₂ = 61.6 ± 0.9 wt%; Na₂O + K₂O = 5.47 wt%). Finally, a synthetic rhyolite composition was synthesized in order to determine S solubility at high SiO₂ contents (i.e., 73.2 ± 0.9 wt%) and relatively alkali-rich melt compositions (Table 1). The starting materials (except the natural rocks), were prepared by combining oxide and carbonate powders in appropriate proportions, crushing into fine powder under ethanol for 1 h and decarbonating at 1273 K in a muffle furnace overnight. The starting composition was then reground for 1 h to be used for sulfate solubility experiments. The compositional data presented in Table 1 were obtained after melting the starting compositions at 1673 K for 15 min in air.

Table 1

Electron microprobe analyses (in wt.%) of the fused starting materials. Numbers in parentheses represents 1 σ uncertainties on the last digit. b.d.l.: below detection limit. Note fusion was in air and hence Fe₂O₃/FeO probably high.

Composition	SiO ₂	Al ₂ O ₃	MgO	CaO	FeO	TiO ₂	K ₂ O	Na ₂ O	MnO	P ₂ O ₅	Total	n
T-Basalt	47.0(1)	16.4(1)	4.3(1)	9.4(1)	10.3(2)	3.33(4)	1.87(3)	4.68(4)	0.21(2)	(1.24) ^a	98.7	10
Lunar Basalt	42.3(2)	11.9(1)	7.5(1)	9.6(1)	16.9(1)	8.34(6)	0.20(3)	0.88(2)	0.58(2)	–	98.2	10
NIB	49.6(1)	14.6(1)	8.7(1)	12.4(1)	9.0(1)	0.92(2)	0.21(6)	2.25(6)	0.17(5)	(0.30)	98.2	10
Nephelinite	41.7(1)	14.2(1)	8.0(1)	13.9(1)	9.9(1)	2.68(1)	3.21(3)	3.95(4)	2.45(2)	–	99.9	8
Andac	61.6(9)	19.0(9)	2.0(2)	4.1(3)	4.9(3)	1.04(4)	4.60(9)	0.87(3)	b.d.l.	–	98.1	8
B-A	53.9(5)	14.6(2)	9.4(2)	9.9(2)	6.4(1)	0.61(1)	1.34(5)	2.79(6)	b.d.l.	–	99.0	8
Andesite	61.1(6)	18.0(2)	3.5(1)	6.9(2)	3.9(1)	0.61(1)	1.19(4)	4.07(6)	b.d.l.	–	99.2	10
Basanite	43.8(1)	10.9(1)	13.1(1)	9.4(1)	11.5(1)	2.28(3)	1.89(2)	3.94(4)	0.18(5)	(1.45) ^b	98.4	10
T-Phonolite	53.3(9)	22.9(9)	1.9(1)	4.8(3)	4.4(1)	1.50(6)	3.64(9)	7.77(9)	b.d.l.	–	100.4	8
Rhyolite	73.2(9)	14.8(9)	0.3(1)	1.0(1)	1.1(4)	0.31(5)	6.08(9)	2.61(7)	b.d.l.	–	99.4	8
SLC	39.9(1)	10.9(1)	15.4(1)	17.3(1)	14.4(1)	b.d.l.	b.d.l.	0.13(3)	b.d.l.	–	98.0	8
CMAS1	48.4(1)	16.8(2)	12.4(1)	22.3(1)	b.d.l.	b.d.l.	b.d.l.	b.d.l.	b.d.l.	–	100.1	10
CMAS2	45.5(1)	18.7(1)	17.4(1)	18.4(1)	b.d.l.	b.d.l.	b.d.l.	b.d.l.	b.d.l.	–	100.1	10
CMAS3	50.4(1)	15.6(1)	14.5(1)	19.6(1)	b.d.l.	b.d.l.	b.d.l.	b.d.l.	b.d.l.	–	100.2	10

^a Data from Taracsák et al. (2021).

^b Data from Adam (1990).

2.2. Experimental conditions

The equilibration experiments were performed in a Gero vertical furnace (HTRV 70-250/18) at atmospheric pressure in a controlled Air–SO₂ atmosphere ($f_{O_2} \gg$ FMQ buffer) in order to stabilize sulfate as the principal S species in the silicate melts (Table 2). The gas mix flux in the vertical furnace was controlled by Tylan mass flow controllers and was maintained at a total of 200 cm³.min^{−1} equivalent to a linear velocity of 0.2 cm/s. The different f_{O_2} and f_{S_2} shown in Table 2 were calculated from thermodynamic data for C–S and O-bearing species (Chase, 1985) following the procedure of White et al. (1958). Three different Air/SO₂ ratios were used (i.e., 0.11, 0.60 and 4.00) in order to determine the f_{O_2} and f_{S_2} effects on sulfate solubility in silicate melts at a fixed temperature (1573 K; Table 2). The gas mixture flux was maintained for 10 min prior to each experiment because this corresponds to the time needed to reach the f_{O_2} and thus gas mix equilibration in an atmospheric furnace (Boulliung et al., 2020). Under these oxidizing conditions platinum dissolves relatively little Fe (e.g., Sugawara, 1999) and can be used as a support for the starting material during the experiments. Between 5 and 10 mg of each starting composition were suspended in the furnace on a 0.25 mm diameter platinum wire loop and stuck to the loop using paraffin oil. Up to 7 experimental charges were hung at the same time on a Pt chandelier suspended from a silica rod.

In order to determine the effect of temperature on sulfate solubility, we used 7 different temperatures ranging from 1473 to 1773 K (with 50 K increments) at a fixed Air/SO₂ ratio (i.e., 0.60; Table 2). Katsura and Nagashima (1974) performed S equilibration experiments using ~50–100 mg of starting material (Hawaiite and tholeiite basalt) and determined that steady state was reached after ~3–6 h at 1523 and 1573 K. Since we used only about 1/5–1/10 as much starting material as in Katsura and Nagashima (1974), we anticipated much shorter equilibration times than they observed. The time required for gas–melt equilibration was therefore determined by running Fe-free, high Ca and lower Ca, Fe-bearing compositions (CMAS1 and NIB respectively) from 1 h to 15 h at 1673 K. The results show that constant S content for the Fe-free composition is reached after 4 h (Fig. 1; Table S1) at this temperature and that only 1 h is required for the NIB (Fe-bearing) composition. This difference of equilibration times may plausibly be related to the substantial difference in equilibrium S contents between the two compositions (Fig. 1).

Given these results and to ensure a close approach to equilibrium, we used a minimum equilibration time of 6 h at 1723 and 1773 K and 10 h at lower temperatures (Table 2). The samples

were quenched under the same atmosphere, in the cold area at the top of the vertical furnace. After the experiment, the quenched glasses were mounted in epoxy and polished. The samples were carbon coated for electron microprobe analysis and gold coated for SIMS analysis.

2.3. Analyses

The major element compositions and the S contents of the glasses were determined by electron microprobe analysis at the University of Oxford, Department of Earth Sciences, using a Cameca SX-Five-FE operating at 45 nA and 15 kV with a spot size of 10 μ m. The standards used for the silicate glass compositions were natural albite (Si, Al, Na), andradite (Ca, Fe), magnesium oxide (Mg), manganese (Mn), sanidine (K) and barite (S as S⁶⁺ valence). Counting times were a minimum of 30 s peak and 15 s background for all elements except for Na and K, for which 20 s peak and 10 s background were used to reduce the element migration rates induced by the beam (see Research Data section for more details on standards and spectrometers used in this study). For sulfur, 80 s peak and 40 s background were used to obtain a detection limit of ~60 ppm. A secondary S standard of L17 glass (1320 ppm S, Nash et al 2019 see Research Data section) was used to ensure consistency with earlier results on glasses containing reduced S (Nash et al 2019). Between 15 and 40 points were analyzed on each sample in order to check for glass homogeneity. For the lowest S contents (i.e., <60 ppm) we performed *in-situ* SIMS measurements using the CAMECA IMS 1270 E7 SIMS at the Centre de Recherches Pétrographiques et Géochimiques (Nancy, France) operating with a 10 kV Cs⁺ primary ion beam, a current of ~10 nA, and a nominal mass resolution of ~4,000. The primary standards used for the SIMS study are natural basaltic glasses: Etna-0 (15 ppm S); 60,701 (700 ppm S); 47,979 (760 ppm S) and CY82-29-3 V (1010 ppm S) (full analyses in Research Data section). We found very good agreement between EPMA and SIMS results on glasses containing between 120 and 1450 ppm S using the primary SIMS calibration (Fig. S1; Table S2). Synthetic glasses from this study (i.e., Lunar basalt; CMAS1; CMAS3; Hmandesite; andesite; nephelinite and basanite) previously analyzed by electron microprobe and with S contents ranging from 80 to 700 ppm were used as secondary standards to complete the calibration. The analyses were focused on three different isotope measurements: ¹⁸O, ³²S and ²⁸Si. The calibration line fitted the signal of ³²S/²⁸Si as a function of the S contents of the standards. Uncertainties on S contents (2 σ) are \leq 30% between 10 and 100 ppm, and 50–100% below 10 ppm.

Table 2

Run conditions and gas mixtures for the different S equilibration experiments of this study at $P = 1$ atm. The conditions to study the temperature effect on sulfur solubility were with a Air/SO₂ ratio of 0.60. The f_{O_2} and f_{S_2} parameters were determined using NIST and JANAF thermochemical tables.

Temperature (K)	Air	SO ₂	Air/SO ₂	log(f_{O_2})	ΔFMQ	log(f_{S_2})	t (h)
1473	37.5	62.5	0.6	−1.10	7.2	−16.22	10
1523	37.5	62.5	0.6	−1.10	6.6	−15.38	10
1573	37.5	62.5	0.6	−1.10	6.1	−14.6	10
1573	10	90	0.11	−1.68	5.5	−13.13	10
1573	80	20	4	−0.77	6.5	−15.87	10
1623	37.5	62.5	0.6	−1.10	5.6	−13.86	10
1673	37.5	62.5	0.6	−1.10	5.2	−13.16	10
1723	37.5	62.5	0.6	−1.10	4.7	−12.51	8
1773	37.5	62.5	0.6	−1.10	4.3	−11.89	6

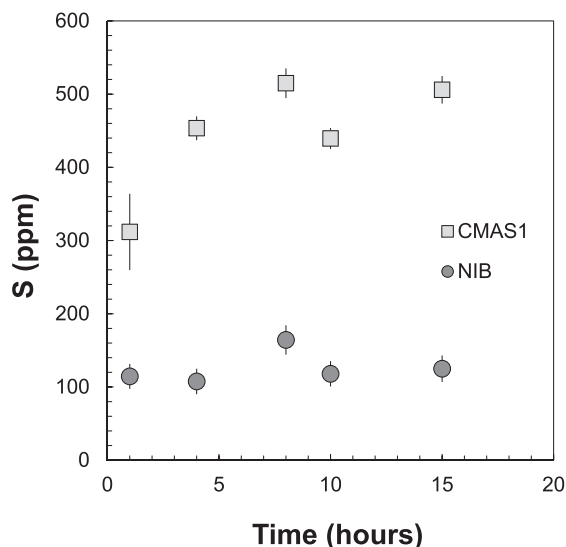


Fig. 1. Time series experiments at 1673 K/1 atm with Air/SO₂ = 0.6, aimed at determining the time required to reach equilibrium sulfur solubility in two different melts, i.e., an Fe-free (CMAS1) and an Fe-bearing (NIB).

3. Results

3.1. Compositions of products

Partially crystallized final run products are excluded from the following discussion and tables because of the impact of crystallization on the final major element composition (e.g., compositions with a liquidus temperature <1523 K are excluded from the 1473 and 1523 K experimental data). The compositions of the quenched run products, i.e., glass only, were little different from those of the starting materials (Table 3). Despite the presence of platinum, used as supporting wire loops, the iron loss was generally low (<13% relative; Fig. 2A and Table 3). The only significant changes were the losses and gains of small amounts of alkali elements (Na₂O and K₂O) during some experiments (Fig. 2B and Table 3) due to gaseous exchange between samples and with the furnace environment. This phenomenon is well known in 1 atmosphere experiments (O'Neill, 2005) and cannot be completely eliminated while keeping samples open to equilibration with the gas mixture.

3.2. Sulfur abundances and sulfate capacities of the glasses

Sulfur abundances obtained by EPMA and SIMS are summarized in Table 3. Following the approach of Fincham and Richardson

Table 3

Major oxide compositions (in wt. %), average sulfur contents (in ppm) and sulfate capacity of the glasses after equilibration experiments. Major oxide compositions and S contents greater than 60 ppm were determined by EPMA and S contents ≤60 ppm were determined by SIMS. The sulfate capacity was calculated according to the Eq. (3). Numbers in parentheses represent 1 σ uncertainties on the last(s) digit(s). b.d.l.: below detection limit. Note high f_{O_2} values and hence ferric/ferrous.

Sample	Temperature (K)	SiO ₂	Al ₂ O ₃	MgO	CaO	FeO	TiO ₂	K ₂ O	Na ₂ O	MnO	P ₂ O ₅	SO ₄	Total	S (ppm)	Log Cs	n
T-Basalt	1473	49.1 (2)	16.6 (1)	4.3 (1)	9.8 (1)	7.63(9)	2.97 (6)	1.30 (6)	4.28 (9)	0.23 (5)	(1.24) ^a	0.465 (12)	97.9	1550 (40)	9.0 (2)	20 (EPMA)
NIB		49.1 (3)	14.4 (1)	8.5 (1)	12.4 (1)	8.88(9)	0.93 (4)	0.41 (6)	2.41 (5)	0.19 (5)	(0.30)	0.543 (12)	98.1	1810 (40)	9.0 (2)	20 (EPMA)
Nephelinite		43.2 (1)	14.3 (1)	7.9 (1)	14.4 (1)	8.73(4)	2.93 (7)	0.49 (9)	2.58 (6)	2.51 (6)		1.227 (42)	98.3	4090 (140)	9.4 (2)	20 (EPMA)
Basanite		47.2 (1)	12.1 (1)	10.4 (5)	10.7 (2)	9.30(9)	2.55 (7)	0.58 (6)	2.92 (6)	0.19 (5)	(1.45) ^b	0.771 (36)	98.1	2570 (120)	9.2 (2)	20 (EPMA)
T-Phonolite		57.7 (2)	20.7 (2)	2.0 (1)	4.6 (1)	4.88(7)	1.64 (5)	2.62 (5)	6.03 (9)	0.14 (6)		0.219 (15)	100.1	730(50)	8.6 (2)	30 (EPMA)
Lunar Basalt	1523	47.0 (5)	13.0 (1)	8.0 (1)	11.0 (1)	11.07 (36)	5.35 (40)	0.24 (7)	1.68 (6)	0.49 (6)		0.150 (3)	98.0	500(10)	8.0 (2)	20 (EPMA)
NIB		50.1 (1)	14.8 (1)	8.7 (1)	12.3 (1)	9.10(6)	0.92 (6)	0.24 (7)	2.09 (7)	0.18 (5)	(0.30)	0.246 (6)	99.0	820(20)	8.3 (2)	30 (EPMA)
Nephelinite		43.3 (9)	14.6 (1)	8.1 (2)	13.8 (9)	9.81(9)	2.75 (9)	0.47 (9)	2.51 (9)	2.42 (9)		0.570 (78)	98.4	1900 (260)	8.6 (2)	20 (EPMA)
B-A		55.3 (2)	14.4 (1)	8.9 (1)	9.5 (1)	5.94(7)	0.62 (6)	1.47 (7)	3.01 (6)	b.d.l.		0.162 (48)	99.3	540 (160)	8.1 (2)	20 (EPMA)
Andesite		62.2 (3)	18.0 (2)	3.3 (1)	6.6 (1)	3.53(6)	0.61 (7)	1.25 (7)	4.83 (6)	b.d.l.		0.029 (12)	100.3	95(40)	7.3 (2)	20 (EPMA)
Basanite		46.1 (9)	11.7 (1)	12.2 (1)	10.1 (2)	10.88 (92)	2.41 (5)	0.49 (6)	2.95 (6)	0.19 (7)	(1.45) ^b	0.393 (12)	99.0	1310 (40)	8.5 (2)	20 (EPMA)

(continued on next page)

Table 3 (continued)

Sample	Temperature (K)	SiO ₂	Al ₂ O ₃	MgO	CaO	FeO	TiO ₂	K ₂ O	Na ₂ O	MnO	P ₂ O ₅	SO ₄	Total	S (ppm)	Log Cs	n
T-Phonolite		57.5 (2)	21.5 (3)	2.0 (1)	4.6 (1)	4.9(7)	1.66 (8)	2.42 (6)	5.34 (9)	0.14 (7)		0.147 (9)	100.2	490(30)	8.0 (2)	40 (EPMA)
SLC		43.4 (2)	11.6 (1)	12.1 (3)	19.9 (1)	10.67 (55)	b.d.l.	b.d.l.	0.56 (7)	b.d.l.		0.951 (21)	99.2	3170 (70)	8.8 (2)	20 (EPMA)
T-Basalt	1573	48.5 (1)	16.9 (1)	4.5 (1)	9.6 (1)	10.77 (5)	3.60 (5)	0.29 (3)	3.39 (4)	0.23 (3)	(1.24) ^a	0.069 (6)	99.0	230(20)	7.3 (1)	20 (EPMA)
Lunar Basalt		42.9 (1)	12.0 (1)	7.7 (1)	10.0 (2)	15.14 (19)	7.44 (5)	b.d.l.	2.00 (9)	0.57 (3)		0.066 (6)	97.8	220(20)	7.3 (1)	15 (EPMA)
NIB		49.5 (1)	14.7 (1)	8.8 (1)	12.2 (1)	9.1(1)	0.93 (2)	0.14 (1)	2.49 (5)	0.17 (2)	(0.30)	0.135 (6)	98.5	450(20)	7.6 (1)	20 (EPMA)
Nephelinite		41.5 (1)	14.4 (1)	8.3 (1)	14.3 (1)	10.68 (8)	2.93 (5)	0.22 (7)	2.33 (7)	2.72 (7)		0.246 (9)	97.6	820(30)	7.9 (1)	20 (EPMA)
Andac		66.1 (9)	15.5 (6)	1.8 (2)	3.2 (2)	4.10(9)	0.93 (7)	4.85 (9)	1.87 (4)	b.d.l.		0.011 (3)	98.4	35(10)	6.5 (1)	5 (SIMS)
B-A		54.3 (1)	14.1 (1)	9.2 (1)	9.6 (1)	6.22(5)	0.60 (6)	1.13 (5)	3.07 (6)	b.d.l.		0.111 (6)	98.4	370(20)	7.5 (1)	20 (EPMA)
Andesite		62.2 (1)	17.0 (1)	3.3 (1)	6.5 (1)	3.53(7)	0.63 (7)	1.38 (6)	4.73 (7)	b.d.l.		0.018 (3)	99.3	59(10)	6.7 (1)	5 (SIMS)
Basanite		45.7 (1)	11.5 (1)	13.5 (1)	9.7 (1)	11.7(1)	2.45 (2)	b.d.l.	2.09 (4)	0.20 (4)	(1.45) ^b	0.135 (6)	98.5	450(20)	7.6 (1)	20 (EPMA)
T-Phonolite		57.7 (2)	20.6 (1)	2.1 (1)	4.8 (1)	4.92(8)	1.66 (7)	2.44 (5)	6.28 (8)	0.15 (5)		0.066 (3)	100.6	220(10)	7.3 (1)	20 (EPMA)
SLC		42.0 (1)	10.8 (1)	14.1 (1)	18.2 (1)	11.86 (6)	b.d.l.	b.d.l.	0.58 (5)	b.d.l.		0.474 (6)	98.0	1579 (20)	8.2 (2)	15 (EPMA)
Rhyolite		70.2 (9)	16.4 (9)	0.3 (1)	1.1 (2)	1.09(7)	0.32 (5)	6.93 (9)	2.47 (19)	b.d.l.		0.004 (3)	98.9	14(9)	6.1 (3)	5 (SIMS)
CMAS1		47.6 (1)	16.9 (1)	11.9 (1)	21.9 (1)	b.d.l.	b.d.l.	b.d.l.	0.90 (1)	b.d.l.		0.582 (7)	99.8	1940 (25)	8.2 (2)	20 (EPMA)
CMAS2		45.0 (1)	20.1 (1)	14.1 (1)	19.2 (1)	b.d.l.	b.d.l.	b.d.l.	0.79 (3)	b.d.l.		0.456 (9)	99.6	1520 (30)	8.1 (2)	20 (EPMA)
CMAS3		49.1 (1)	15.3 (1)	14.4 (1)	19.1 (1)	b.d.l.	b.d.l.	b.d.l.	0.78 (4)	b.d.l.		0.435 (9)	99.5	1450 (30)	8.1 (1)	20 (EPMA)
T-Basalt	1623	48.3 (1)	16.4 (1)	4.3 (1)	9.5 (1)	10.63 (5)	3.46 (6)	0.93 (4)	4.03 (6)	0.24 (4)	(1.24) ^a	0.045 (3)	99.0	150(10)	6.8 (2)	20 (EPMA)
Lunar Basalt		42.7 (1)	11.1 (1)	7.0 (1)	9.3 (1)	16.89 (8)	8.39 (5)	0.11 (5)	1.68 (5)	0.51 (4)		0.019 (7)	97.7	64(22)	6.4 (2)	5 (SIMS)
NIB		49.6 (1)	14.7 (1)	8.6 (1)	12.4 (1)	9.21(5)	0.94 (7)	0.20 (5)	2.26 (6)	0.19 (5)	(0.30)	0.063 (3)	98.4	210(10)	6.9 (2)	20 (EPMA)
Nephelinite		42.1 (1)	14.6 (1)	8.2 (1)	14.3 (1)	10.67 (6)	2.90 (6)	0.14 (4)	2.17 (5)	2.75 (6)		0.123 (6)	98.0	410(20)	7.2 (2)	20 (EPMA)
Andac		65.6 (5)	15.9 (2)	1.4 (1)	3.4 (1)	4.03(6)	0.92 (4)	5.06 (5)	1.99 (9)	b.d.l.		0.008 (3)	98.3	25(9)	6.0 (2)	5 (SIMS)
B-A		54.3 (2)	14.4 (1)	9.0 (1)	9.6 (1)	6.43(4)	0.58 (6)	1.10 (4)	2.88 (5)	b.d.l.		0.051 (6)	98.3	170(20)	6.8 (2)	20 (EPMA)
Andesite		62.4 (1)	17.0 (1)	3.2 (1)	6.5 (1)	3.49(4)	0.61 (6)	1.55 (5)	5.19 (5)	b.d.l.		0.020 (4)	99.9	65(12)	6.4 (2)	5 (SIMS)
Basanite		45.6 (1)	11.4 (1)	13.5 (1)	9.7 (1)	11.76 (6)	2.44 (7)	0.13 (6)	2.49 (6)	0.20 (5)	(1.45) ^b	0.084 (3)	98.9	280(10)	7.0 (2)	20 (EPMA)
T-Phonolite		58.1 (2)	20.6 (1)	2.1 (1)	4.8 (1)	5.01(4)	1.65 (5)	2.08 (5)	6.23 (9)	0.15 (4)		0.039 (3)	100.7	130(10)	6.7 (2)	25 (EPMA)
SLC		40.5 (1)	10.6 (1)	15.0 (1)	17.4 (1)	13.39 (8)	b.d.l.	b.d.l.	0.64 (7)	b.d.l.		0.264 (6)	97.8	880(20)	7.5 (2)	20 (EPMA)
Rhyolite		72.8 (9)	14.4 (8)	0.3 (1)	1.0 (2)	1.15(9)	0.31 (4)	7.48 (9)	1.51 (9)	b.d.l.		0.003 (3)	98.9	10(9)	5.6 (2)	5 (SIMS)
CMAS1		48.0 (1)	16.5 (1)	11.9 (1)	21.7 (1)	b.d.l.	b.d.l.	b.d.l.	0.74 (6)	b.d.l.		0.267 (6)	99.1	890(20)	7.5 (2)	20 (EPMA)
CMAS2		44.9 (1)	19.0 (1)	16.0 (1)	18.5 (1)	b.d.l.	b.d.l.	b.d.l.	0.71 (6)	b.d.l.		0.216 (6)	99.3	720(20)	7.4 (2)	20 (EPMA)
CMAS3		49.4 (1)	15.3 (1)	14.3 (1)	19.2 (1)	b.d.l.	b.d.l.	b.d.l.	0.95 (5)	b.d.l.		0.213 (6)	99.5	710(20)	7.4 (2)	20 (EPMA)
T-Basalt	1673	49.0 (2)	17.0 (1)	4.5 (1)	9.6 (1)	10.65 (7)	3.58 (5)	0.24 (5)	3.79 (4)	0.23 (4)	(1.24) ^a	0.018 (5)	99.8	59(16)	6.0 (2)	20 (EPMA)
Lunar Basalt		41.2 (4)	11.5 (1)	7.3 (2)	9.1 (5)	17.03 (75)	8.66 (9)	b.d.l.	2.04 (9)	0.68 (5)		0.026 (14)	97.5	87(48)	6.2 (2)	20 (EPMA)
NIB		49.7 (1)	14.8 (1)	8.8 (1)	12.2 (1)	9.04(6)	0.93 (4)	0.15 (2)	2.42 (7)	0.18 (3)	(0.30)	0.036 (6)	98.5	120(20)	6.3 (2)	20 (EPMA)
Nephelinite		42.8 (1)	14.8 (1)	8.3 (1)	13.6 (1)	10.47 (9)	2.97 (6)	0.11 (4)	2.17 (5)	2.65 (6)		0.06 (6)	97.9	200(30)	6.5 (2)	20 (EPMA)
Andac		65.6 (4)	16.5 (1)	1.6 (2)	3.7 (2)	4.21(9)	0.98 (4)	4.41 (9)	2.25 (5)	b.d.l.		0.005 (3)	99.3	15(9)	5.4 (3)	5 (SIMS)
B-A		54.8	14.7	9.1	9.7	5.99(7)	0.60	0.85	3.16	b.d.l.		0.030	98.9	100(20)	6.2	20

Table 3 (continued)

Sample	Temperature (K)	SiO ₂	Al ₂ O ₃	MgO	CaO	FeO	TiO ₂	K ₂ O	Na ₂ O	MnO	P ₂ O ₅	SO ₄	Total	S (ppm)	Log Cs	n
Andesite		(1) 62.6 (3)	(1) 18.0 (1)	(1) 3.3 (1)	(1) 6.7 (1)	3.55(6)	(9) 0.63 (4)	(6) 1.23 (5)	(9) 4.20 (9)	b.d.l.		(6) 0.011 (3)	100.2	37(10)	(2) 5.8 (2)	(EPMA) 5 (SIMS)
Basanite		45.9 (1)	11.5 (1)	13.6 (1)	9.7 (1)	11.66 (8)	2.47 (4)	b.d.l.	2.23 (9)	0.20 (5)	(1.45) ^b	0.042 (6)	98.8	140(20)	6.4 (2)	20 (EPMA)
SLC		39.4 (1)	10.7 (1)	15.5 (1)	16.7 (1)	14.7(1)	b.d.l.	b.d.l.	0.63 (5)	b.d.l.		0.117 (6)	97.8	390(20)	6.8 (2)	20 (EPMA)
Rhyolite		73.2 (9)	14.8 (9)	0.31 (4)	1.0 (2)	1.15(9)	0.32 (3)	6.05 (9)	2.58 (9)	b.d.l.		0.003 (3)	99.4	8(9)	5.1 (2)	5 (SIMS)
CMAS1		48.1 (1)	16.5 (1)	12.3 (1)	21.7 (1)	b.d.l.	b.d.l.	b.d.l.	0.90 (4)	b.d.l.		0.132 (3)	99.7	440(10)	6.9 (2)	20 (EPMA)
CMAS2		45.1 (1)	18.6 (1)	17.5 (1)	17.5 (1)	b.d.l.	b.d.l.	b.d.l.	1.06 (5)	b.d.l.		0.120 (6)	99.9	400(20)	6.8 (2)	20 (EPMA)
CMAS3		49.6 (1)	15.4 (1)	14.3 (1)	19.2 (1)	b.d.l.	b.d.l.	b.d.l.	1.29 (5)	b.d.l.		0.108 (9)	99.9	360(30)	6.8 (2)	20 (EPMA)
T-Basalt	1723	49.0 (2)	16.8 (1)	4.4 (1)	9.7 (9)	10.02 (9)	3.4(6)	0.59 (7)	4.04 (9)	0.21 (6)	(1.24) ^a	0.014 (3)	99.4	46(10)	5.6 (2)	5 (SIMS)
Lunar Basalt NIB		41.9 (1)	11.7 (1)	7.3 (1)	9.4 (1)	15.95 (9)	8.56 (6)	0.17 (7)	3.09 (9)	0.55 (7)		0.016 (3)	98.6	52(10)	5.6 (2)	5 (SIMS)
Nephelinite		50.0 (1)	14.8 (1)	8.8 (1)	12.3 (1)	8.85(7)	0.90 (6)	0.24 (6)	3.01 (8)	0.18 (6)	(0.30)	0.030 (6)	99.4	100(20)	5.9 (2)	20 (EPMA)
Andac		42.5 (1)	14.8 (1)	8.4 (1)	14.6 (1)	10.20 (7)	2.8(6)	b.d.l.	2.70 (7)	2.49 (7)		0.042 (6)	98.5	140(20)	6.0 (2)	20 (EPMA)
B-A		66.0 (3)	16.5 (1)	1.7 (1)	3.4 (1)	3.82(7)	0.94 (6)	4.33 (6)	2.76 (6)	b.d.l.		0.004 (3)	99.4	13(9)	5.0 (3)	5 (SIMS)
Andesite		55.4 (1)	14.6 (1)	9.2 (1)	9.6 (1)	5.50(6)	0.59 (5)	0.75 (7)	4.01 (7)	b.d.l.		0.019 (5)	99.7	62(16)	5.7 (2)	5 (SIMS)
Basanite		62.3 (1)	17.9 (1)	3.3 (1)	6.6 (1)	3.28(7)	0.59 (6)	0.97 (7)	5.74 (5)	b.d.l.		0.007 (3)	100.7	24(9)	5.3 (2)	5 (SIMS)
T-Phonolite		46.1 (2)	11.5 (1)	13.8 (1)	9.9 (1)	11.37 (9)	2.39 (6)	0.16 (6)	2.72 (9)	0.19 (6)	(1.45) ^b	0.036 (3)	99.6	120(10)	6.0 (2)	20 (EPMA)
SLC		57.7 (2)	22.2 (1)	2.1 (1)	4.8 (1)	4.81(7)	1.64 (6)	1.60 (7)	5.83 (8)	0.14 (9)		0.023 (6)	100.8	75(21)	5.8 (2)	5 (SIMS)
Rhyolite		39.7 (1)	10.9 (1)	15.6 (1)	17.1 (1)	14.22 (8)	b.d.l.	b.d.l.	1.15 (6)	b.d.l.		0.075 (9)	98.8	250(30)	6.3 (2)	25 (EPMA)
CMAS1		75.0 (9)	13.3 (6)	0.3 (1)	0.9 (2)	0.93(7)	0.29 (6)	5.81 (9)	2.97 (9)	b.d.l.		0.002 (3)	99.5	8(9)	4.8 (7)	5 (SIMS)
CMAS2		48.1 (1)	16.7 (1)	12.1 (1)	22.2 (1)	b.d.l.	b.d.l.	b.d.l.	1.38 (6)	b.d.l.		0.093 (6)	100.6	310(20)	6.4 (2)	20 (EPMA)
CMAS3		45.4 (2)	18.8 (2)	17.8 (3)	17.5 (5)	b.d.l.	b.d.l.	b.d.l.	1.44 (6)	b.d.l.		0.078 (6)	101.0	260(20)	6.3 (2)	20 (EPMA)
T-Basalt	1773	50.0 (1)	15.5 (1)	14.5 (1)	19.2 (1)	b.d.l.	b.d.l.	b.d.l.	1.43 (6)	b.d.l.		0.066 (6)	100.6	220(20)	6.2 (2)	20 (EPMA)
Lunar Basalt NIB		49.2 (1)	16.8 (1)	4.4 (1)	9.6 (1)	9.87(8)	3.46 (6)	0.42 (7)	4.65 (8)	0.22 (7)	(1.24) ^a	0.008 (3)	99.8	27(9)	5.0 (2)	5 (SIMS)
Nephelinite		42.3 (1)	11.5 (1)	7.2 (1)	9.4 (1)	16.62 (9)	8.62 (8)	b.d.l.	2.30 (6)	0.62 (7)		0.008 (3)	98.5	25(9)	5.0 (2)	5 (SIMS)
Andac		50.5 (1)	14.9 (1)	8.6 (1)	12.4 (1)	8.47(6)	0.92 (7)	b.d.l.	3.23 (6)	0.17 (6)	(0.30)	0.012 (3)	99.5	39(10)	5.2 (2)	5 (SIMS)
B-A		41.8 (2)	14.6 (1)	8.4 (1)	14.3 (3)	10.27 (9)	2.90 (6)	b.d.l.	3.45 (9)	2.62 (6)		0.054 (3)	98.3	180 (100)	5.9 (2)	30 (EPMA)
Andesite		66.1 (3)	16.2 (1)	1.5 (1)	3.3 (1)	4.06(5)	0.97 (6)	4.34 (6)	3.06 (9)	b.d.l.		0.004 (3)	99.6	14(9)	4.7 (2)	5 (SIMS)
Basanite		53.8 (3)	14.6 (1)	9.1 (1)	9.8 (1)	6.00(7)	0.60 (6)	0.59 (5)	5.33 (9)	b.d.l.		0.013 (3)	99.8	44(10)	5.2 (2)	5 (SIMS)
T-Phonolite		62.3 (1)	17.9 (1)	3.4 (1)	6.6 (1)	3.37(5)	0.63 (5)	1.12 (5)	5.33 (9)	b.d.l.		0.006 (3)	100.6	20(9)	4.9 (2)	5 (SIMS)
SLC		46.6 (1)	11.7 (1)	13.6 (1)	9.9 (1)	11.04 (8)	2.41 (7)	b.d.l.	2.96 (7)	0.20 (7)	(1.45) ^b	0.015 (3)	99.9	49(10)	5.3 (2)	5 (SIMS)
Rhyolite		58.4 (2)	22.0 (1)	2.1 (1)	4.8 (1)	4.69(9)	1.72 (6)	1.21 (5)	4.39 (7)	0.15 (5)		0.010 (3)	99.5	32(10)	5.1 (2)	5 (SIMS)
CMAS1		40.3 (1)	11.0 (1)	15.3 (1)	17.2 (1)	13.83 (7)	b.d.l.	b.d.l.	0.96 (7)	b.d.l.		0.045 (6)	98.6	150(20)	5.8 (2)	20 (EPMA)
CMAS2		74.8 (8)	15.1 (7)	0.3 (1)	0.9 (1)	1.14(9)	0.32 (6)	4.10 (1)	3.52 (9)	b.d.l.		0.002 (3)	100.2	8(9)	4.5 (7)	5 (SIMS)
CMAS3		48.4 (1)	16.9 (1)	12.0 (1)	22.2 (1)	b.d.l.	b.d.l.	b.d.l.	1.23 (7)	b.d.l.		0.048 (6)	100.7	160(20)	5.8 (2)	30 (EPMA)
Andesite		45.6 (1)	19.0 (1)	17.3 (1)	17.7 (1)	b.d.l.	b.d.l.	b.d.l.	1.12 (7)	b.d.l.		0.036 (6)	100.7	120(20)	5.7 (2)	30 (EPMA)
Basanite		48.9 (1)	15.2 (1)	14.2 (1)	18.9 (1)	b.d.l.	b.d.l.	b.d.l.	2.98 (6)	b.d.l.		0.036 (3)	100.2	120(9)	5.7 (2)	30 (EPMA)

^a Data from Taracsák et al. (2021).^b Data from Adam (1990).

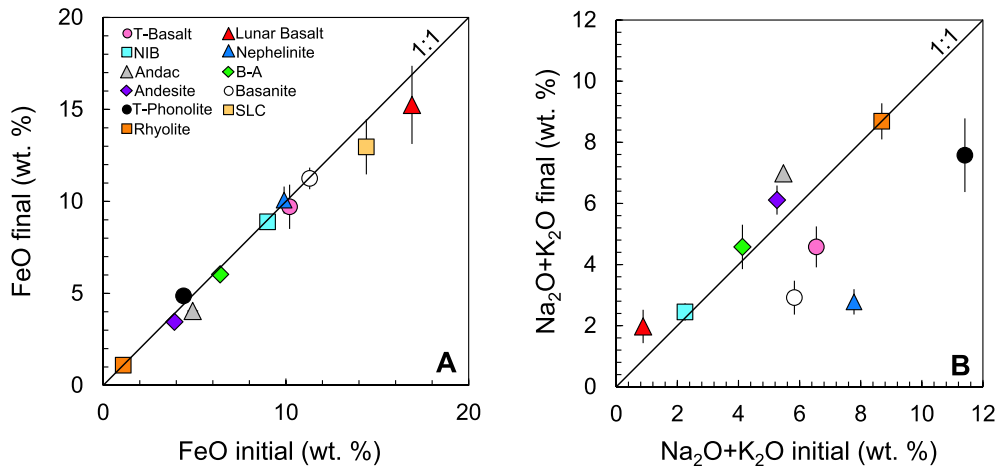


Fig. 2. Evolution of (A) the FeO and (B) the alkali ($\text{Na}_2\text{O} + \text{K}_2\text{O}$) contents during the experiments for different melt compositions. Data for all temperatures at Air/SO_2 of 0.6 are collected into individual points. The initial value refers to the concentration before the experiment. The final concentrations were obtained from the average measured concentrations (Table 3).

(1954) the sulfate capacity defined by Eq. (3) and expressed in terms of weight % S was calculated for each run product. The results from 1473 to 1773 K are reported in Table 3. Uncertainties on the values of $\log C_{\text{S}6+}$ were calculated by combining the standard deviations of the S contents with 0.1 log unit uncertainties attributed to $f\text{O}_2$ and $f\text{S}_2$.

The data presented in Table 3 indicate an increase in S concentration with decreasing temperature at fixed Air/SO_2 . For example, with Air/SO_2 of 0.6 the NIB composition has a sulfur content at 1573 K of 820 ± 20 ppm against 450 ± 20 ppm at 1623 K (Fig. 3). Note that the effect of temperature shown in the figure is, in effect, a combination of temperature and $f\text{S}_2$ effects at fixed $f\text{O}_2$ ($10^{-1.1}$) but changing $f\text{O}_2$ of the FMQ buffer. The effect of temperature is also observed in sulfate capacity for all compositions (Fig. 4). As an example, the $\log C_{\text{S}6+}$ of the andesite increases from 4.9 ± 0.2 at 1773 K to 7.3 ± 0.2 at 1523 K (Fig. 4).

In addition to the strong temperature dependence, Fig. 4 shows that sulfate capacity depends on composition. At fixed temperature

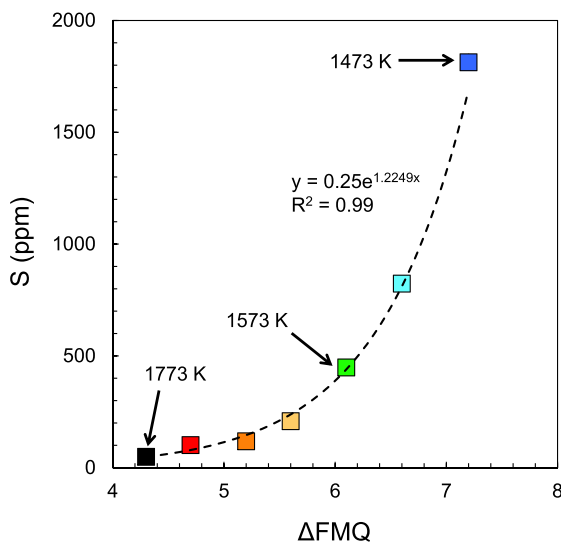


Fig. 3. Sulfur concentration of Icelandic basalt (NIB) as function of oxygen fugacity ($\log f\text{O}_2$ relative to the FMQ buffer) and temperature (from 1473 to 1773 K). The dotted line represents a fitted exponential function. The S content increases by a factor ~ 2 when the temperature decreases by 50 K. The $\log f\text{O}_2$ is constant for all the data shown on this figure (i.e., $\log f\text{O}_2 = -1.1$).

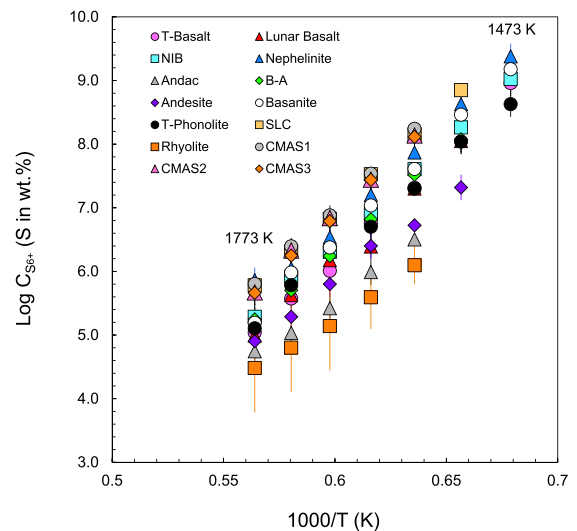


Fig. 4. Temperature effect on log of sulfate capacity for different melt compositions derived from experiments at a $\log f\text{O}_2$ of -1.10 .

the sulfate capacity in NIB basalt is, for example, always higher than in the andesite (Fig. 4) with values of $\log C_{\text{S}6+}$ of 7.6 ± 0.1 and 6.7 ± 0.1 respectively at 1573 K. The next step is to quantify these qualitative compositional effects.

3.3. A quantitative description of sulfate capacity as a function of temperature and composition

Fig. 5 illustrates the effects of major element composition on S, as sulfate, solubility at 1573 K for gas of Air/SO_2 of 0.6. The data show no apparent correlation between S content and the concentrations of SiO_2 , Al_2O_3 and FeO in the silicate melt (Fig. 5A–C). In contrast there is a very good correlation between S content and CaO concentration (Fig. 5D) that is also clearly seen in a plot of sulfate capacity $\log C_{\text{S}6+}$ versus CaO (Fig. 6). At 1573 K, for example, $\log C_{\text{S}6+}$ values increase from 6.1 ± 0.3 for the rhyolite (0.9% CaO) to 8.2 ± 0.2 for the CMAS1 (22.2% CaO).

We determined the combined compositional and temperature effects on sulfate capacity by fitting $\log C_{\text{S}6+}$ (from Table 3) to a

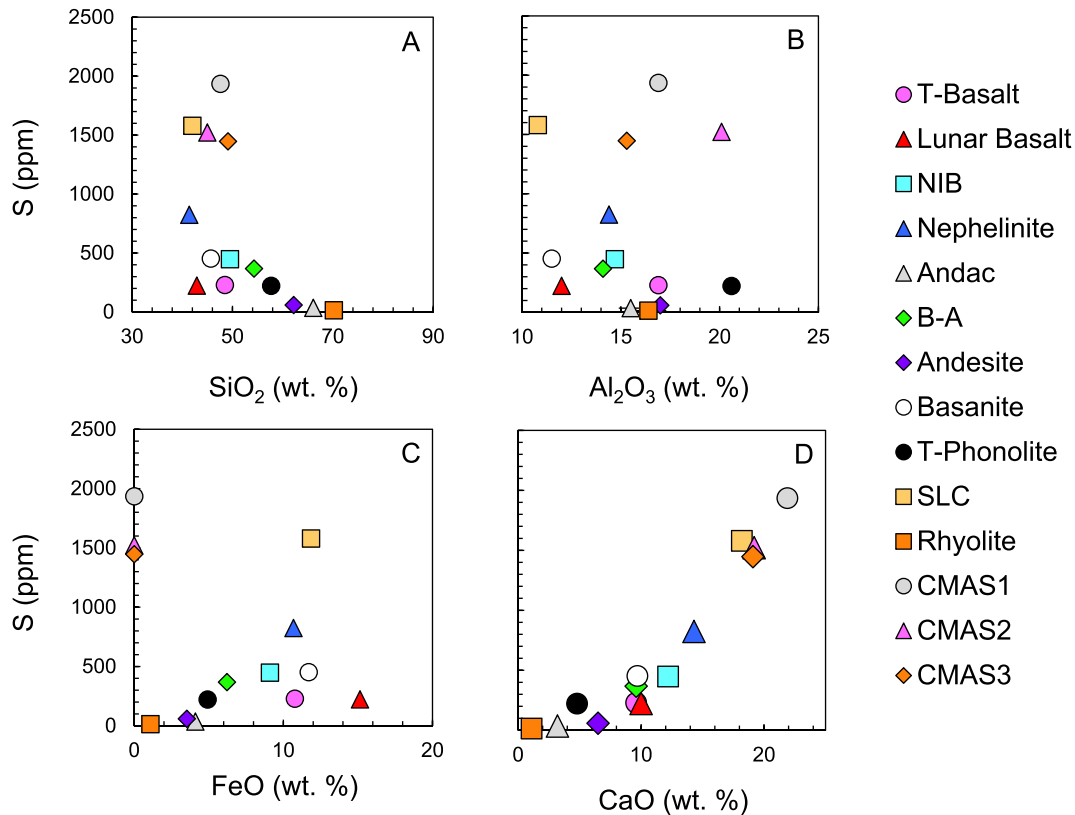


Fig. 5. Major oxide concentrations as functions of the sulfur contents for each melt composition at fixed temperature, 1573 K and $\log f_{O_2}$ of -1.10 . Data were taken from Table 3.

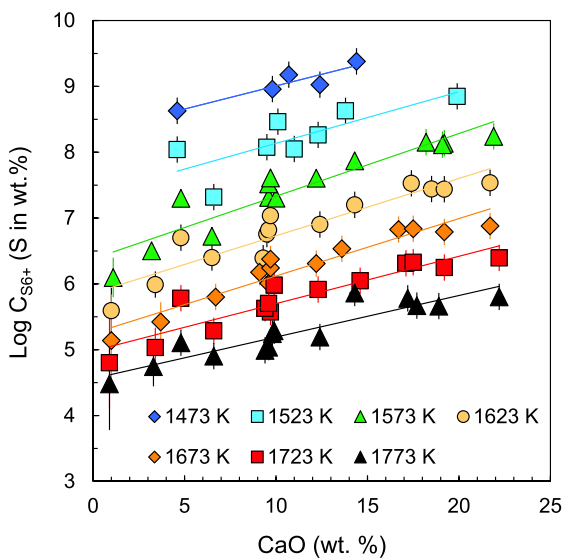


Fig. 6. Sulfate capacity plotted as a function of the CaO (wt.%) content at different temperatures (1473 to 1773 K). The CaO content corresponds to the final composition after the experiment (data from Table 3).

combination of terms in oxide mole fraction on a single cation basis (SiO_2 , FeO , $AlO_{1.5}$ etc) and reciprocal temperature. The form of the fit equation is derived from reciprocal solution theory (O'Neill and Mavrogenes, 2002, 2022). The method involved stepwise linear regression using the SPSS statistical package with terms which did not pass the F-test at $\alpha = 0.05$ excluded. Because $\log C_{S6+}$ is directly related to $\log K$ (equilibrium constant) the temperature

dependence is, as with $\log K$, reciprocal temperature. In order to ensure that the compositional terms approach zero at infinite temperature the oxide mole fractions, were also divided by temperature. This approach resulted in the following fit equation (5):

$$\log C_{S6+} = -12.659 + (3692X_{CaO} - 7592X_{SiO_2} - 13736X_{TiO_2} + 3762X_{AlO_{1.5}} + 34483)/T \quad (5)$$

The standard error of the fit is 0.154 and R^2 is 0.985. All 6 parameters have $\text{mod}(t)$ values greater than 2.5 and p values below 0.02 indicating significance at greater than 95% level (see supplementary data SPSS_Sulfate_Regression). Fig. 6 shows that the temperature and the CaO content of the melt are the most important parameters correlated with $\log C_{S6+}$. By taking into account only these two parameters, and by using the same linear regression approach, we obtain the following equation (6):

$$\log C_{S6+} = -12.806 + (14502X_{CaO} + 30375)/T \quad (6)$$

with a standard error of the fit of 0.211 and $R^2 = 0.970$ indicating a very good correlation as observed for equation (5).

3.4. Henry's Law Tests

In order to apply our results to natural compositions we must ensure either that sulfate capacity ($\log C_{S6+}$) is independent of S content (Henry's Law) or that, if composition-dependence is observed, we are able to characterize it adequately. Our tests for Henry's Law behavior involved performing experiments at 3 different Air:SO₂ ratios (Table 2), 37.5:62.5; 10:90 and 80:20 and calculating $\log C_{S6+}$ for each composition under the 3 different conditions. Henry's Law is obeyed if $\log C_{S6+}$ is independent of the S content of the product glasses (Fig. 7). In Fig. 7A we show the results for 3 compositions which illustrate significant ranges

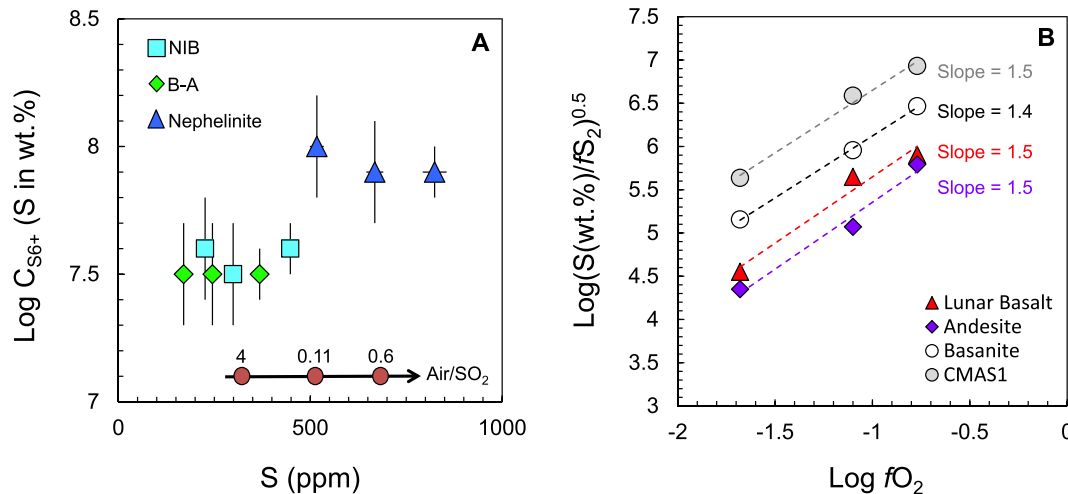


Fig. 7. (A) Shows the values of $\log C_{S6+}$ determined at 1 atm pressure/1573 K for 3 different Air/SO₂ gas ratios (i.e., 0.11, 0.6 and 4) and 3 different melt compositions. The arrow indicates the order (left to right) of the Air/SO₂ ratio for each composition. (B) $\log(S(\text{wt.}\%)/fS_2)^{0.5}$ as function of the $\log fO_2$ at 1 atm pressure/1573 K for 4 different melt compositions. The slopes of 1.5 show that the stoichiometry of reaction (1) is obeyed. Henry's Law is also shown to be obeyed because $\log C_{S6+}$ is independent of S content for any specific major element composition (A and B) and because the stoichiometry of reaction (1) is respected (B).

in S content, nephelinite, Icelandic basalt and high-Mg Andesite and as can be seen, all 3 exhibit Henrian behavior within the ± 0.2 uncertainties in $\log C_{S6+}$. The plot of $\log \frac{S(\text{wt.}\%)}{(fS_2)^{1/2}}$ vs $\log fO_2$ (Fig. 7B) for 4 different melt compositions with a wide range of polymerization (NBO/T from 0.5 to 1.5), shows slopes of ~ 1.5 in good agreement with the stoichiometry of Reaction (1) and consistent with Henry's law. Note that there is no discernable effect of changing Fe^{3+}/Fe^{2+} with changing fO_2 in the range we have used. In summary, Henrian behavior applies within uncertainty to all 12 melts which we have investigated under all three gas ratios (Tables 3 and 4) indicating that we can assume that $\log C_{S6+}$ is constant under most conditions relevant to nature.

4. Discussion

4.1. Comparison with previous experimental data and calculation model

The data obtained in this study can readily be compared with previous experimental results on sulfate solubility in silicate melts and sulfate capacity calculation models. The data at 1 bar obtained by Nash et al. (2019) and Katsura and Nagashima (1974) diverge somewhat from our fit equation (Fig. 8). We believe that this is due to the large uncertainties associated with the low S contents (i.e., <100 ppm) they measured and thus, on the sulfate capacity. By using a wet chemical method to determine S content, Katsura and Nagashima (1974) obtained a detection limit of 10 ppm, which is very close to the S contents of the samples (i.e., ≤ 60 ppm) indicating a large, but unknown uncertainty in $\log C_{S6+}$. The data of Nash et al. (2019) overlap the predicted line within analytical uncertainty (Fig. 8). The high pressure data of Lesne et al. (2015) ranging from 264 to 2084 bar can be compared with this study because of the negligible effect of pressure on $\log C_{S6+}$ (Moretti and Ottonello, 2005; Lesne et al., 2015; Xu and Li, 2021). The $\log C_{S6+}$ data from the Lesne et al. (2015) study are close to the values predicted from our equation (Fig. 8) but spread across the 1:1 line. Because water contents of silicate melts appear to affect sulfate capacities (e.g., Moretti and Ottonello, 2005; see section 4.3), the range in $\log C_{S6+}$ observed by Lesne et al. (2015) is likely due to the water contents of the melts (0.7 to 3.5 wt% H₂O). It appears,

however that H₂O does not affect all compositions significantly because the data of Cl  mente et al. (2004) on hydrous rhyolites (1.8–5.8 wt% H₂O) at 2000 bar and 1273 K are in excellent agreement with our model (Fig. 8).

Moretti and Ottonello (2005) present a global model for S solubility and S^{2-} and S^{6+} capacities as functions of pressure, temperature, fO_2 , fS_2 and melt composition. When compared in the ranges of fO_2 , fS_2 , melt composition, temperature and pressure of our data, however, we find that the Moretti and Ottonello (2005) CTSFG model overestimates S solubility and hence the $\log C_{S6+}$ by approximately one order of magnitude (Fig. S3). This may be due to the relative lack of experimental data available to Moretti and Ottonello (2005), in the field where sulfate dominates the S speciation in the melt.

Our data were also compared with the recent study from O'Neill and Mavrogenes (2022) on the sulfate capacities of silicate melts (Fig. S4). By using a similar experimental approach (i.e., 1 bar and a temperature range of 1473–1773 K) but with different melt compositions, O'Neill and Mavrogenes (2022) obtained an equation showing 7 compositional parameters (i.e., Na, Mg, Al, K, Ca, Mn and Fe^{2+}). The data are globally in good agreement with this study and show a similar temperature effect on sulfate capacity.

4.2. Pressure dependence of sulfate capacity and degassing of SO₂ at depth

From Eqs. (4) and (1) we see that the observed compositional dependence of $\log C_{S6+}$ is due to the compositional effects on activities of oxygen ($aO_{2,melt}^{2-}$) and sulfate SO_4^{2-} because K is, by definition composition-independent. The pressure dependence of $\log C_{S6+}$ should, however, from Eq. (4) be closely related to the pressure dependence of $\log K$:

$$\frac{\partial \log K}{\partial P} = \frac{-\Delta V^0}{2.303RT} \quad (7)$$

In Eq. (7) ΔV^0 is the volume change of reaction (1) in which SO_4^{2-} replaces O^{2-} , and R is the gas constant (8.3145 J K⁻¹ mol⁻¹). Thomas and Wood (2021) showed that the apparent volume difference between $2Cl^-$ and O^{2-} in melts is very close to the volume difference between $CaCl_2$ and CaO at 298 K/1bar (i.e., for a basalt

Table 4

Major oxides compositions (in wt.%), sulfur contents (in ppm) and sulfate capacity of final glass products obtained at 1573 K and for two different Air/SO₂ ratios (i.e., 4.00 and 0.11). Numbers in parentheses represent 1σ uncertainties on the last(s) digit(s). b.d.l.: below detection limit.

Composition	Air/ SO ₂	SiO ₂	Al ₂ O ₃	MgO	CaO	FeO	TiO ₂	K ₂ O	Na ₂ O	MnO	P ₂ O ₅	SO ₄	Total	S (ppm)	Log Cs	n
T-Basalt	4	47.6 (1)	16.4 (1)	4.3(1)	9.4(1)	10.43 (9)	3.39 (8)	1.41 (7)	4.27 (7)	0.22 (6)	(1.24) ^a	0.054(6)	98.6	180(20)	7.5 (2)	30 (EPMA)
Lunar Basalt		44.7 (1)	11.9 (1)	7.6(1)	10.0 (1)	14.57 (8)	6.84 (9)	b.d.l.	1.40 (6)	0.66 (7)		0.027(3)	97.7	90(10)	7.2 (2)	25 (EPMA)
NIB		50.1 (1)	14.8 (1)	8.7(1)	12.4 (1)	9.09(7)	0.92 (8)	b.d.l.	2.09 (7)	b.d.l.	(0.30)	0.069(6)	98.5	230(20)	7.6 (2)	30 (EPMA)
Nephelinite		41.9 (1)	14.5 (1)	8.1(2)	14.2 (1)	10.54 (7)	2.88 (7)	0.45 (7)	2.69 (7)	2.58 (6)		0.156(6)	98.1	520(20)	8.0 (2)	30 (EPMA)
B-A		54.4 (1)	14.4 (1)	9.1(1)	9.6(1)	6.36(8)	0.62 (6)	1.44 (8)	3.06 (6)	b.d.l.		0.051(6)	99.0	170(20)	7.5 (2)	30 (EPMA)
Andesite		61.8 (1)	17.7 (1)	3.2(1)	6.5(1)	3.52(8)	0.61 (7)	2.01 (7)	4.76 (7)	b.d.l.		0.021(6)	100.1	70(20)	7.1 (2)	25 (EPMA)
Basanite		45.6 (1)	11.3 (1)	13.4 (1)	9.7(1)	11.66 (7)	2.39 (7)	0.28 (6)	2.56 (7)	b.d.l.	(1.45) ^b	0.102(6)	98.5	340(20)	7.8 (2)	30 (EPMA)
T-Phonolite		55.8 (3)	22.1 (1)	2.1(1)	5.0(1)	5.15(7)	1.69 (7)	2.60 (7)	5.80 (9)	b.d.l.		0.051(6)	100.2	170(20)	7.5 (2)	30 (EPMA)
SLC		42.5 (1)	11.0 (1)	14.0 (1)	18.7 (1)	11.81 (9)	b.d.l.	b.d.l.	b.d.l.	b.d.l.		0.243(6)	98.3	810(20)	8.2 (2)	20 (EPMA)
CMAS1		48.1 (1)	17.0 (1)	12.0 (1)	22.4 (1)	b.d.l.	b.d.l.	b.d.l.	b.d.l.	b.d.l.		0.297(6)	99.8	990(20)	8.3 (2)	30 (EPMA)
CMAS2		46.2 (1)	20.0 (1)	13.8 (2)	19.6 (1)	b.d.l.	b.d.l.	b.d.l.	b.d.l.	b.d.l.		0.180(9)	99.9	600(30)	8.1 (2)	30 (EPMA)
CMAS3		50.3 (1)	15.4 (1)	14.5 (1)	19.2 (1)	b.d.l.	b.d.l.	b.d.l.	b.d.l.	b.d.l.		0.207(6)	99.6	690(20)	8.1 (2)	30 (EPMA)
T-Basalt	0.11	47.7 (1)	16.3 (1)	4.3(1)	9.4(1)	10.29 (7)	3.39 (6)	1.19 (7)	4.0(7)	0.21 (6)	(1.24) ^a	0.075(6)	98.3	250(20)	7.5 (2)	40 (EPMA)
Lunar Basalt		43.5 (1)	11.7 (1)	7.6(1)	9.9(1)	15.59 (7)	7.66 (8)	b.d.l.	0.91 (7)	0.58 (5)		0.030(5)	97.5	100(15)	7.1 (2)	20 (EPMA)
NIB		49.9 (2)	14.8 (1)	8.7(1)	12.3 (1)	9.06(9)	0.92 (7)	b.d.l.	2.19 (6)	b.d.l.	(0.30)	0.090(6)	98.3	300(20)	7.5 (2)	40 (EPMA)
Nephelinite		42.1 (1)	14.6 (1)	8.2(1)	14.3 (1)	10.42 (9)	2.85 (7)	0.31 (6)	2.46 (8)	2.59 (7)		0.201(6)	97.9	670(20)	7.9 (2)	40 (EPMA)
Andac		67.2 (9)	15.8 (6)	1.4(1)	3.2(2)	3.94(7)	0.94 (8)	4.97 (9)	0.96 (9)	b.d.l.		0.0141 (7)	98.4	47(23)	6.7 (3)	5 (SIMS)
B-A		54.9 (1)	14.5 (1)	9.2(1)	9.6(1)	6.40(6)	0.61 (6)	1.21 (6)	2.77 (7)	b.d.l.		0.072(6)	99.3	240(20)	7.5 (2)	45 (EPMA)
Andesite		62.1 (2)	17.7 (1)	3.3(1)	6.7(1)	3.58(6)	0.62 (5)	1.61 (6)	4.24 (6)	b.d.l.		0.018(6)	99.9	60(20)	6.9 (2)	5 (SIMS)
Basanite		45.8 (1)	11.4 (1)	13.5(1)	9.8(1)	11.43 (6)	2.41 (6)	0.28 (6)	2.46 (7)	b.d.l.	(1.45) ^b	0.117(6)	98.7	390(20)	7.7 (2)	50 (EPMA)
T-Phonolite		57.1 (4)	21.8 (2)	2.0(1)	4.6(1)	4.77(9)	1.64 (6)	2.55 (7)	5.58 (7)	b.d.l.		0.057(6)	100.1	190(20)	7.3 (2)	40 (EPMA)
SLC		41.7 (1)	11.0 (1)	13.9 (2)	18.8 (1)	12.32 (6)	b.d.l.	b.d.l.	b.d.l.	b.d.l.		0.300(5)	98.0	1000 (15)	8.1 (2)	20 (EPMA)
CMAS1		48.1 (1)	16.8 (1)	11.8 (1)	22.4 (1)	b.d.l.	b.d.l.	b.d.l.	b.d.l.	b.d.l.		0.354(6)	99.4	1180 (20)	8.2 (2)	40 (EPMA)
CMAS2		45.7 (1)	19.7 (4)	14.3 (7)	19.6 (6)	b.d.l.	b.d.l.	b.d.l.	b.d.l.	b.d.l.		0.276 (12)	99.6	920(40)	8.0 (2)	20 (EPMA)
CMAS3		50.2 (1)	15.7 (1)	14.4 (1)	19.4 (1)	b.d.l.	b.d.l.	b.d.l.	b.d.l.	b.d.l.		0.249(6)	99.9	830(20)	8.0 (2)	20 (EPMA)

^a Data from Taracsák et al. (2021).

^b Data from Adam (1990).

17.3 cm³/mol as opposed to 17.03 cm³/mol). We therefore estimated the volume change of sulfate dissolution using the volume difference at 298 K between CaSO₄ (45.94 cm³ mol⁻¹) and CaO (16.764 cm³ mol⁻¹) (Robie et al., 1978), which yields for the pressure dependence of sulfate capacity (*P* in MPa):

$$\log C_{S_{(P,T)}}^{6+} = \log C_{S_{(1\text{bar})}}^{6+} - \frac{(P - 0.1) \times 1.5237}{T} \quad (8)$$

By combining equations (3) and (8) we obtain the following relationship:

$$\log SO_{4\text{melt},P,T}^{2-} = \log C_{S_{(1\text{bar})}}^{6+} + \frac{1}{2} \log f_{S_2} + \frac{3}{2} \log f_{O_2} - \frac{(P - 0.1) \times 1.5237}{T} \quad (9)$$

In order to apply Eq. (9) to sulfate concentration and degassing of SO₂ in a volcanic edifice or deeper in the crust we need to convert the sulfate dissolution reaction (1) into one involving SO₂. We did this by using log *K* values for reaction (10) from the NIST-JANAF database (<https://janaf.nist.gov>):



In the temperature range 900–2000 K the equilibrium constant for reaction (10) (with all components as gas) fits closely (within 0.002 log units) to the equation:

$$\log K_{(10)} = \frac{18887}{T} - 3.8064 \quad (11)$$

We now subtract reaction (10) from reaction (1).

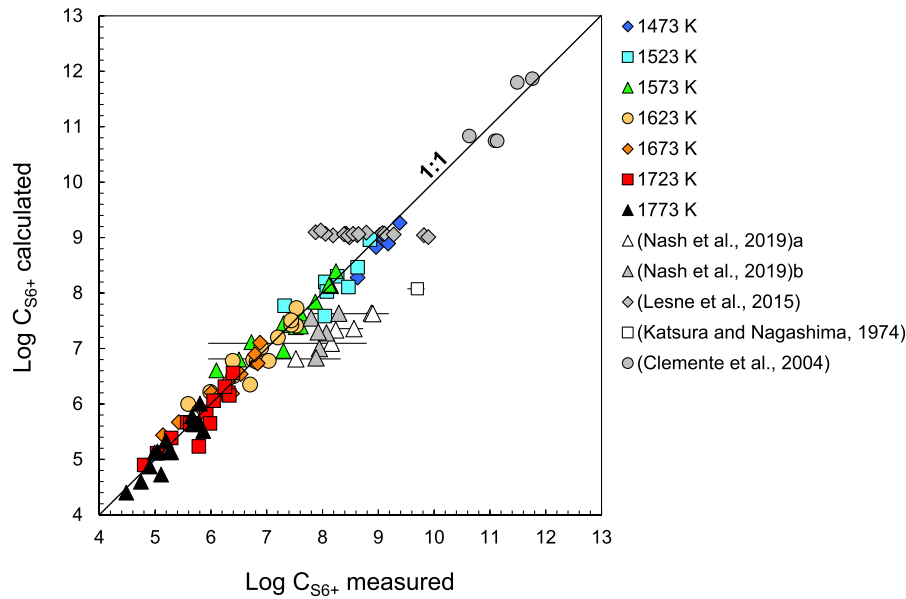
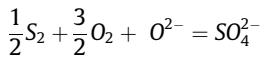


Fig. 8. Sulfate capacity measured from experimental data as function of the log C_{S6+} calculated using Equation (5). The data from Nash et al. (2019) were obtained for different melt compositions at 1573 K and 1 bar under, (a) FMQ+1.60 and (b) FMQ+1.21 redox conditions. Uncertainties associated with the Nash et al. (2019) data are only shown for the data obtained at FMQ+1.60 (uncertainties in the data obtained at FMQ+1.21 are much higher because the S contents are <4 ppm). The data from Lesne et al. (2015) are for experiments using three different basalt compositions at 1473 K, for pressures ranging from 264 to 2084 bar and $fO_2 > \text{FMQ}+1.3$. The data point from Katsura and Nagashima (1974) corresponds to tholeiite basalt melted at $T = 1523$ K, $P = 1$ bar and $fO_2 = \text{FMQ}+4.09$. Cl  mente et al. (2004) data are for hydrous rhyolitic melts at $T = 1273$ K, $P = 2$ kbar and $fO_2 \geq \text{FMQ}+2.2$.



to give the reaction:



This means that we can eliminate the fugacity of S_2 from our expression for sulfate capacity by combining log C_{S6+} from Eq. (3) with the equilibrium constant for reaction (10).

We then obtain the sulfate content in terms of the fugacities of SO_2 and O_2 :

$$\log SO_{4melt}^{2-} = \log C_{S6+} - \log K_{(10)} + \log fSO_2 + \frac{1}{2} \log fO_2 - \frac{1.5237}{T} (P - 0.1) \quad (13)$$

or as:

$$\log SO_{4melt}^{2-} = \log C_{S6+} - \left(\frac{18887}{T} - 3.8064 \right) + \log fSO_2 + \frac{1}{2} \log fO_2 - \frac{1.5237}{T} (P - 0.1) \quad (14)$$

Note that we are expressing sulfate capacity as weight% S, not weight% SO_4^{2-} . By using Eq. (14), we can estimate for a given S content of a magma, under oxidizing conditions (i.e. $\geq \text{FMQ}+2$), the fraction of S degassed as SO_2 into a coexisting gas phase (the phase with the lowest density in equilibrium with silicate melt, Verhoogen, 1949) during magma ascent. If we fix T and the initial S content of the melt and define fO_2 relative to a common buffer such as FMQ (Frost, 1991) the log fSO_2 is fixed from Eq. (14). We then convert fSO_2 to mole fraction of SO_2 in the gas phase using:

$$fSO_2 = P \times \phi_{SO_2} \times X_{SO_2} \quad (15)$$

In Eq. (15) ϕ_{SO_2} is the fugacity coefficient of SO_2 in a mixed fluid phase of mole fraction X_{SO_2} which we assume to be dominated by H_2O but which may contain up to 30% CO_2 . We derived values of

ϕ_{SO_2} for our calculations by assuming a fluid of 0.95 mol fraction H_2O and 0.05 SO_2 . We then calculated the fugacity coefficients in the mixture from the Modified Redlich Kwong (MRK) equation of state using parameters for H_2O and CO_2 from Holloway (1977) and for SO_2 from (Prausnitz et al., 1999). We also checked that addition of up to 30% CO_2 to the fluid has negligible impact on ϕ_{SO_2} at the highest pressures (250 MPa) used in the simulation described below. This enables us to calculate the degassing paths of melts of known initial oxygen fugacity and known initial S content as they ascend through the crust.

Let us consider a basaltic magma of the same composition as the Icelandic basalt at an initial fO_2 of 2 log fO_2 units above FMQ and an initial S content of 0.35% (as sulfate). This melt will start to degas SO_2 in an H_2O -dominated fluid as the melt approaches H_2O -saturation. We chose to start the calculation at 250 MPa and calculated the saturated water content at 1473 K (5.4%), using the empirical model of Moore et al. (1998). We used this H_2O saturation model to calculate the amount of H_2O exsolved from the melt into the gas phase during decompression, but made no explicit correction for the effect of H_2O on sulfate capacity. The latter is discussed further below. Because degassing of sulfur is known to cause changes in fO_2 (Gaillard et al., 2011; Moussallam et al., 2014; Gaillard et al., 2015; Brounce et al., 2017), we calculated the fO_2 effects of SO_2 degassing using the Kress and Carmichael, (1991) model for Fe oxidation state. In this example, when the total amount of S dissolved as sulfate (i.e., 0.35% S) is degassed as SO_2 , the fO_2 should increase due to oxidation of FeO to Fe_2O_3 . We calculate that the effect is an increase of +1.34 units in log fO_2 from +2 to +3.34 log units relative to FMQ. The calculation assumes all S is degassed as SO_2 and all H as H_2O and has not taken account of the minor amounts of H_2 , H_2S and S_2 in the gas phase. These would act to further increase fO_2 .

The simulation (Fig. 9) shows that the Icelandic basalt composition will have degassed more than 50% of its S by the time pressure reaches 190 MPa and there will be none left at 20 MPa. In Fig. 9 we present S degassing scenarios for an andesite (from Carmichael et al. 1974) together with the Icelandic basalt (NIB) for initial S

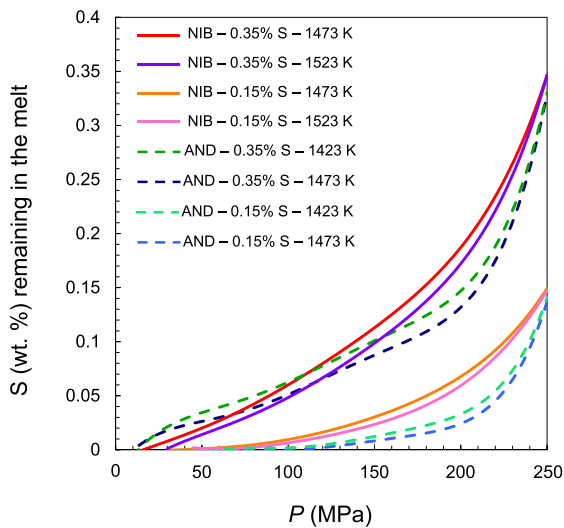


Fig. 9. Depicts simulations of upwelling melts which begin to degas an H₂O-rich fluid at 250 MPa. The amounts of S (weight%) remaining in the melt are shown as functions of the pressure. Two compositions were used, Icelandic basalt, NIB and an andesite composition AND, from Carmichael, (1974), with 0.15 and 0.35 wt% S in the initial melt. These simulations take into account the evolution of the magma redox conditions during degassing and begin with an initial $fO_2 = FMQ+2$ at 250 MPa.

contents of 0.15 and 0.35%. The amounts of S were selected as being representative of the range (1000–4000 ppm) estimated for primary arc magmas (Zimmer et al., 2010; Muth and Wallace, 2021). If we were to add 1500 ppm CO₂ to our initial melt, then using VolatileCalc2.0 (Newman and Lowenstern, 2002) for both basalt and rhyolite, degassing would begin at pressures higher than 250 MPa and S would be degassed even more rapidly than shown in Fig. 9. Since CO₂ is much less soluble than H₂O in magmas at low pressure, about 85% of the CO₂ is degassed by 250 MPa and 98% by 200 MPa with <4% CO₂ in the gas phase. Therefore the effects of CO₂ on our calculated degassing paths should be small in the pressure range of Fig. 9. In constructing Fig. 9, temperatures for isothermal ascent and degassing were selected to be above the liquidus for the entirety of the sulfur degassing path. Liquidus temperatures dry and with H₂O were obtained from MELTS software (MELTS_v1.2.0). Our degassing calculations (Fig. 9) show that SO₂ partitions strongly into an H₂O-rich phase as suggested by previous studies (e.g., Keppler, 1999) and that for these two melts, the total amount of S initially present in the magma will have degassed by about 50 MPa if the melt initially contained 0.15% S and by about 20 MPa if the initial content were 0.35 wt%. All of the calculations take into account the fO_2 change during SO₂ degassing as discussed above, using the Kress and Carmichael (1991) equations. If, for comparison, we were to hold fO_2 constant at 2 log fO_2 units above FMQ during the degassing process instead of allowing it to increase, the S contents of the melts would decline more rapidly with decreasing pressure (supplementary Fig. S2) and S would be completely degassed at between 50 and 100 MPa. This is because decreasing fO_2 (by holding at FMQ+2 log units) leads to decreasing sulfate solubility (Eq. (13)) and hence more efficient degassing of SO₂. The conclusion based on our experiments, that SO₂ starts degassing at relatively high pressures during ascent and is virtually completely lost by 50 MPa is consistent with experimental results on the compositions of fluids coexisting with basalt (Lesne et al., 2011). The latter indicate strong degassing of S at pressures below 150 MPa under oxidizing conditions and demonstrate that Cl is retained in the melt to much shallower depths than S. Thomas

and Wood (2021) also found that Cl should be retained in basaltic melts to much lower pressures (<2 MPa) than we find for SO₂. Degassing of S and Cl at the Souffrière Hills volcano, Montserrat (Edmonds et al., 2001) is similarly consistent with evolution of SO₂ from deep (5–7 km, 125–175 MPa) crustal magma chambers while Cl is emitted during ascent and eruption of the andesite magma.

The redox conditions of Mariana arc basalts based on Fe³⁺/Fe²⁺ measurements on olivine-hosted melt inclusions (Brounce et al., 2014) range between FMQ+1 and FMQ+1.6 log units. Under these fO_2 conditions S is dominantly incorporated as sulfate in silicate melts (Metrich and Clocchiatti, 1996; Jugo et al., 2010; Baker and Moretti, 2011; Nash et al., 2019) and this constraint enables us to estimate the extents of S degassing that the melts have experienced and their effects. As an example we take a submarine andesitic glass (1885-6) with 110 ppm S from the Mariana Arc (Alt et al., 1993). From Eq. (4) we calculate a log C_{S6+} of 8.8 ± 0.2 for this melt at 1473 K. The most S-rich melt inclusions from the Mariana Arc system show S concentrations ranging from 592 to 2115 ppm (Kelley et al., 2010). An initial concentration in the middle of this range of 1100 ppm would, at 1473 K, degas SO₂ (Eq. (14)) at a minimum pressure of 47 MPa and increase oxygen fugacity by ~0.6 log fO_2 units as S concentration decreases to 110 ppm (Fig. 10). A similar melt containing 2–3% H₂O at 1423 K would, with log C_{S6+} of 9.5 and an initial concentration of 2000 ppm S degas SO₂ at a minimum pressure of 155 MPa with an increase of 1.0 in log fO_2 . In each case we are constraining the minimum pressure by assuming a pure SO₂ fluid, but in practice fluids will be H₂O-rich and degassing will start deeper as shown in Fig. 9. As before, however, our results are consistent with both previous high-pressure experiments and with field observations. The important addition that we have made to the previously available data is that we have constrained the temperature and composition dependences of SO₂ solubility in natural silicate melts.

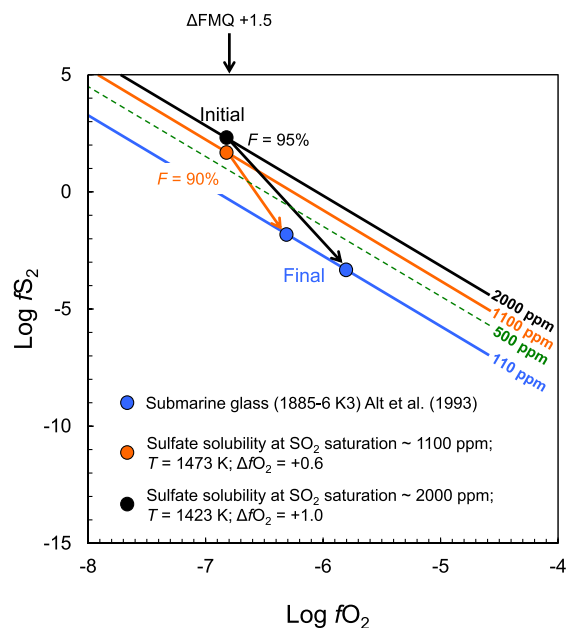


Fig. 10. Sulfur solubility as a function of log fO_2 and log fS_2 for the andesitic submarine glass 1885-6 which contains 110 ppm S. If, prior to degassing, the melt contained 2000 ppm S the pressure of degassing must have been at least 155 MPa with degassing causing a 1 log unit increase in fO_2 (see text). If the melt had initially contained 1100 ppm S the corresponding minimum pressure is 47 MPa and change in fO_2 0.6 log units.

4.3. Effect of water on sulfate capacity

Thus far we have made no provision for the potential effects of H₂O in the melt on sulfate capacity. The available evidence however, is that they are small and composition-dependent. The data of Clémente et al. (2004) on hydrous rhyolite at 1273 K and 2000 bar are, for example in excellent agreement with our model (Fig. 8) without any adjustment for the H₂O content of the melt. Fig. 11 shows the effects of H₂O on sulfate capacity calculated from the Moretti and Ottonello (2005) CTSFG model at 1473 K for our Icelandic basalt (NIB) and at 1423 K for andesite (AND). As can be seen, sulfate capacity increases slightly and then decreases as water is added up to 5 wt%, but the overall change is small, 0–0.4 in log C_{S6+}. The recent work of Xu and Li (2021) on an andesite composition also yielded small decreases in sulfate capacity with increasing water content broadly consistent with the model for andesite (Fig. 11). In order therefore to calculate the effects of H₂O in the melt on the degassing simulations presented in Fig. 9, we used the Moretti–Ottonello model to estimate the changes in sulfate capacity caused by moderate amounts (3 and 5 wt%) of H₂O in the melt. In both cases we assumed H₂O saturation at 250 MPa and throughout the degassing path and simply shifted log C_{S6+} for the anhydrous composition by estimated amounts for 3 and 5% H₂O. For the basaltic composition, addition of up to 5 wt% H₂O in the melt decreases log C_{S6+} causing S to degas more efficiently during magma ascent (Fig. 12). In the case of andesite, these amounts of water increase sulfate capacity which results in the andesite degassing SO₂ less easily and hence at lower pressures than those shown in Fig. 9. The model suggests, therefore that, depending on major element composition, water in the melt can either accelerate or delay degassing of SO₂. However, more experimental data are clearly needed to better constrain the effects of water on log C_{S6+} and on S degassing processes.

Further support for our assumption that H₂O-effects on sulfate capacity are small are provided by the hydrothermal experiments of Fiege et al. (2014) on S partitioning between melt and fluid at an *f*O₂ of FMQ+3. These authors obtained a sulfur partitioning coefficient between fluid and melt (*D*_{S^{fl/m}) of between 100 and 400 for andesitic melt at pressures between 150 and 100 MPa and temperatures of 1303 K. Our calculation at the lowest experimental temperature (i.e., 1473 K) gives a value of *D*_{S^{fl/m} ~ 100 using the anhydrous values of sulfate capacity for the andesite melt. We also}}

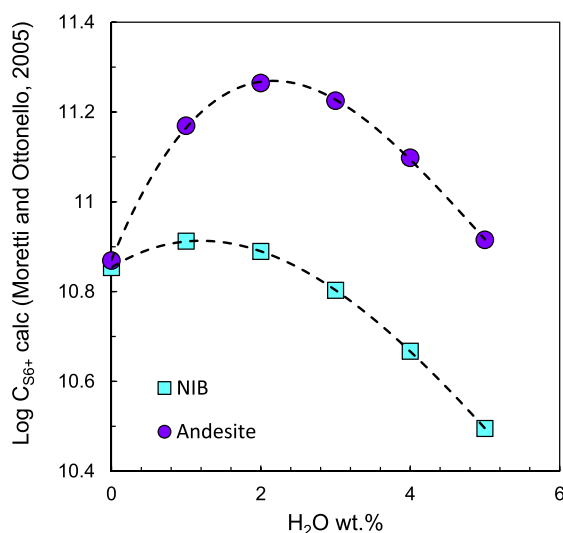


Fig. 11. Calculated change in sulfate capacity as function of the water content in NIB and andesitic melts. The sulfate capacities were calculated at 1473 K (NIB) and 1423 K (Andesite) and 1 bar pressure using Moretti and Ottonello, (2005) CTSFG model.

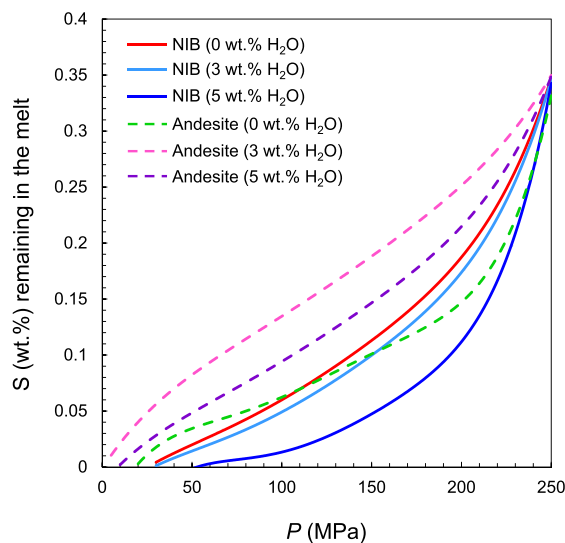


Fig. 12. Simulation of S degassing during magma ascent for NIB and andesite compositions at fixed temperature (i.e., 1473 and 1423 K for the NIB and the andesite respectively) with initially 0.35 wt% S. The effect of water on the sulfate capacity used for this simulation was estimated using the CTSFG model from Moretti and Ottonello (2005). The simulation with 0 wt% H₂O is similar to that shown in Fig. 9. These simulations take into account the evolution of the magma redox conditions during degassing and begin with an initial *f*O₂ = FMQ+2 at 250 MPa.

find that the S partition coefficient should increase with decreasing temperature which would bring our calculation into even better agreement with the Fiege et al. (2014) data at 1303 K.

5. Conclusions

Our study has resulted in a comprehensive description of the temperature and composition dependences of SO₂ solubility in natural silicate melts. This was derived from experiments performed at 1 atmosphere pressure and temperatures of 1473–1773 K in which 14 different silicate melts were exposed to high fugacities of O₂ and SO₂. Under these conditions the sulfur dissolves in the melt predominantly as sulfate (SO₄²⁻) and the equilibrium S species in the gas is SO₂. The sulfur contents of the quenched run products were determined by EPMA and by SIMS for low sulfur contents (<60 ppm S). By performing time series experiments we showed that, at 1673 K with 5–10 mg samples, gas–melt equilibrium is reached after ~4 h in an Fe-free composition and ~1 h in an Icelandic basalt. All further re-equilibration experiments were ≥6 h in duration.

The observed S concentrations were treated using the approach of Fincham and Richardson (1954) in which the equilibrium S contents at the temperature of the experiment are cast as sulfate capacities (C_{S6+}) defined as follows:

$$\log C_{S6+} = \log SO_{4melt}^{2-}(\text{wt.}\%) - \frac{1}{2} \log fS_2 - \frac{3}{2} \log fO_2$$

In this equation *SO*_{4melt}²⁻ refers to the sulfur concentration that we express as weight% S for simplicity, and *f*S₂ and *f*O₂ correspond to the fugacities of sulfur and oxygen respectively. The data show that sulfate capacities are both temperature and major element composition-dependent with S content increasing strongly with decreasing temperature and with increasing CaO content of the melt. In all cases log C_{S6+} was found to be independent of S content within uncertainty. Thus, Henry's Law is obeyed, within uncertainty, in the composition range 0–2000 ppm at 1573 K and potentially to even higher concentrations.

In order to represent the data we used stepwise linear regression to generate the fit equation:

$$\log C_{S^{6+}} = -12.659 + (3692X_{CaO} - 7592X_{SiO_2} - 13736X_{TiO_2} + 3762X_{AlO_{1.5}} + 34483)/T$$

In this equation X_{CaO} , X_{SiO_2} , X_{TiO_2} and $X_{AlO_{1.5}}$ are the mole fractions of CaO, SiO₂, TiO₂ and AlO_{1.5} on a single cation basis. Compositional parameters, which did not pass the F-test at the 95% level, were excluded from the equation. The standard error of the fit is 0.154 and R^2 is 0.985.

We used our equation for $\log C_{S^{6+}}$ to simulate different scenarios for S degassing processes in oxidized magmatic systems. We find that, during magma ascent, degassing of an H₂O-rich fluid in the crust will rapidly strip SO₂ from melts of any composition. For example we find that an ascending melt containing 0.35% S which begins to degas an SO₂-bearing H₂O-rich fluid at 250 MPa will lose 85% of its S by the time the pressure reaches 100 MPa and virtually all by 20 MPa. In the case of a melt initially containing 0.15% S all of the S will have been degassed by the time the pressure has decreased to 50 MPa. These calculations are consistent with the experiments of Lesne et al. (2011) who determined the partitioning of S and Cl from melts into fluids under oxidizing conditions and found that S is strongly degassed from the melt at pressures below 150 MPa. It is also consistent with field observations at Soufrière Hills, Montserrat (Edmonds et al., 2001) which indicate SO₂ degassing from magma at appreciable depth (5–7 km) corresponding to pressures of 125–175 MPa.

Data availability

Data will be made available on request.

Declaration of Competing Interest

The authors declare that they have no known competing financial interests or personal relationships that could have appeared to influence the work reported in this paper.

Acknowledgments

We acknowledge support of the UK Science Technologies and Facilities Council (STFC) through the grant ST/R000999/1. We thank Richard Thomas and Zoltán Taracsák for providing sample materials and Andrew Matzen for assistance with microprobe analyses. We also thank Roberto Moretti for sharing the code for the CTSFG model and Charles Losos for checking our calculations. Johan Villeneuve is gratefully acknowledged for SIMS analyses, as is Gordon Moore for providing a spreadsheet for H₂O-solubility calculations. The manuscript benefitted greatly from reviews by Fabrice Gaillard, Pedro J. Jugo, Roberto Moretti and an anonymous reviewer. Bernard Charlier the Associate Editor, is gratefully thank for his editorial handling and comments.

Appendix A. Supplementary material

Supplementary material to this article can be found online at <https://doi.org/10.1016/j.gca.2022.08.032>.

References

Adam, J., 1990. The geochemistry and experimental petrology of sodic alkaline basalts from Oatlands, Tasmania. *J. Petrol.* 31 (6), 1201–1223.
 Aiuppa, A., Moretti, R., Federico, C., Giudice, G., Gurrieri, S., Liuzzo, M., Papale, P., Shinohara, H., Valenza, M., 2007. Forecasting Etna eruptions by real-time observation of volcanic gas composition. *Geology* 35 (12), 1115–1118.

Aiuppa, A., Bertagnini, A., Métrich, N., Moretti, R., Di Muro, A., Liuzzo, M., Tamburello, G., 2010. A model of degassing for Stromboli volcano. *Earth Planet. Sci. Lett.* 295 (1–2), 195–204.
 Alt, J.C., Shanks III, W.C., Jackson, M.C., 1993. Cycling of sulfur in subduction zones: The geochemistry of sulfur in the Mariana Island Arc and back-arc trough. *Earth Planet. Sci. Lett.* 119 (4), 477–494.
 Baker, D.R., Moretti, R., 2011. Modeling the solubility of sulfur in magmas: a 50-year old geochemical challenge. *Rev. Mineral. Geochem.* 73 (1), 167–213.
 Beermann, O., Botcharnikov, R.E., Holtz, F., Dierich, O., Nowak, M., 2011. Temperature dependence of sulfide and sulfate solubility in olivine-saturated basaltic magmas. *Geochim. Cosmochim. Acta* 75 (23), 7612–7631.
 Botcharnikov, R.E., Linnen, R.L., Wilke, M., Holtz, F., Jugo, P.J., Berndt, J., 2011. High gold concentrations in sulphide-bearing magma under oxidizing conditions. *Nat. Geosci.* 4 (2), 112–115.
 Boulliung, J., Fürti, E., Dalou, C., Tissandier, L., Zimmermann, L., Marrocchi, Y., 2020. Oxygen fugacity and melt composition controls on nitrogen solubility in silicate melts. *Geochim. Cosmochim. Acta* 284, 120–133.
 Brauns, R., 1914. Skapolithführende Auswürflinge aus dem Laacher Seegebiet. *Neues Jahrbuch für Mineralogie, Geologie und Paläontologie* 39, 79–125.
 Brounce, M.N., Kelley, K.A., Cottrell, E., 2014. Variations in $Fe^{3+}/\Sigma Fe$ of Mariana Arc basalts and mantle wedge fO_2 . *J. Petrol.* 55 (12), 2513–2536.
 Brounce, M.N., Stolper, E., Eiler, J., 2017. Redox variations in Mauna Kea lavas, the oxygen fugacity of the Hawaiian plume, and the role of volcanic gases in Earth's oxygenation. *PNAS* 114 (34), 8997–9002.
 Carmichael, I.S., Turner, F.J., Verhoogen, J., 1974. Igneous petrology.
 Carroll, M.R., Rutherford, M.J., 1985. Sulfide and sulfate saturation in hydrous silicate melts. *J. Geophys. Res.: Solid Earth* 90 (S02), C601–C612.
 Carroll, M.R., Rutherford, M.J., 1987. The stability of igneous anhydrite: experimental results and implications for sulfur behavior in the 1982 El Chichón trachyandesite and other evolved magmas. *J. Petrol.* 28 (5), 781–801.
 Chang, J., Audétat, A., 2018. Petrogenesis and metal content of hornblende-rich xenoliths from two Laramide-age magma systems in southwestern USA: insights into the metal budget of arc magmas. *J. Petrol.* 59 (10), 1869–1898.
 Chase Jr., M.W., 1985. JANAF thermochemical tables third edition. *J. Phys. Chem. Ref. Data* 14 (Supplement 1).
 Chen, C., Li, D.T., Wu, T.T., Zhao, Y., Zhao, C.Q., Yang, J.L., Gu, Y.C., 2020. Genesis of gold deposits in the Wulong orefield, Liaodong Peninsula, North China Craton: Constraints from ore deposit geology, REE, and C–H–O–S–Pb isotopes. *Geol. J.* 55 (8), 5914–5933.
 Chowdhury, P., Dasgupta, R., 2019. Effect of sulfate on the basaltic liquidus and sulfur Concentration at Anhydrite Saturation (SCAS) of hydrous basalts—Implications for sulfur cycle in subduction zones. *Chem. Geol.* 522, 162–174.
 Clémence, B., Scaillet, B., Pichavant, M., 2004. The solubility of sulphur in hydrous rhyolitic melts. *J. Petrol.* 45 (11), 2171–2196.
 Costa, F., Scaillet, B., Pichavant, M., 2004. Petrological and experimental constraints on the pre-eruptive conditions of Holocene dacite from Volcán San Pedro (36 S, Chilean Andes) and the importance of sulphur in silicic subduction-related magmas. *J. Petrol.* 45 (4), 855–881.
 Edmonds, M., Pyle, D., Oppenheimer, C., 2001. A model for degassing at the Soufrière Hills Volcano, Montserrat, West Indies, based on geochemical data. *Earth Planet. Sci. Lett.* 186 (2), 159–173.
 Edmonds, M., Aiuppa, A., Humphreys, M., Moretti, R., Giudice, G., Martin, R.S., Martin, R.S., Herd, R.A., Christopher, T., 2010. Excess volatiles supplied by mingling of mafic magma at an andesite arc volcano. *Geochim. Geophys. Geosyst.* 11 (4).
 Fiege, A., Behrens, H., Holtz, F., Adams, F., 2014. Kinetic vs. thermodynamic control of degassing of H₂O–S±Cl-bearing andesitic melts. *Geochim. Cosmochim. Acta* 125, 241–264.
 Fincham, C.J.B., Richardson, F.D., 1954. The behaviour of sulphur in silicate and aluminate melts. *Proc. R. Soc. Lond. Ser. A. Math. Phys. Sci.* 223 (1152), 40–62.
 Frost, R.B., 1991. Introduction to oxygen fugacity and its petrological importance. *Rev. Mineral. Geochem.* 5, 1–16.
 Gaillard, F., Scaillet, B., Arndt, N.T., 2011. Atmospheric oxygenation caused by a change in volcanic degassing pressure. *Nature* 478 (7368), 229–232.
 Gaillard, F., Scaillet, B., Pichavant, M., Iacono-Marziano, G., 2015. The redox geodynamics linking basalts and their mantle sources through space and time. *Chem. Geol.* 418, 217–233.
 Gennaro, M.E., 2017. Sulfur behavior and redox conditions in Etnean hydrous basalts inferred from melt inclusions and experimental glasses Ph. D. thesis. Univ. d'Orléans; Univ. degli studi, Palermo, Italia.
 Grondahl, C., Zajacz, Z., 2017. Magmatic controls on the genesis of porphyry Cu–Mo–Au deposits: the Bingham Canyon example. *Earth Planet. Sci. Lett.* 480, 53–65.
 Holloway, J.R., 1977. Fugacity and activity of molecular species in supercritical fluids. In: *Thermodynamics in Geology*. Springer, Dordrecht, pp. 161–181.
 Huang, R., Keppler, H., 2015. Anhydrite stability and the effect of Ca on the behavior of sulfur in felsic magmas. *Am. Mineral.* 100 (1), 257–266.
 Hubbard, N.J., Gast, P.W., 1971. Chemical composition and origin of nonmare lunar basalts. *Lunar Planet. Sci. Conf. Proceed.*, 2, p. 999.
 Hytönen, K., Schairer, J.F., 1961. *Ann. Rept. Director Geophys. Lab. 1960–1961; in Carnegie Inst. Washington Year Bbook*. 60, 126.
 Jugo, P.J., 2009. Sulfur content at sulfide saturation in oxidized magmas. *Geology* 37 (5), 415–418.
 Jugo, P.J., Luth, R.W., Richards, J.P., 2005. An experimental study of the sulfur content in basaltic melts saturated with immiscible sulfide or sulfate liquids at 1300 °C and 10 GPa. *J. Petrol.* 46 (4), 783–798.

- Jugo, P.J., Wilke, M., Botcharnikov, R.E., 2010. Sulfur K-edge XANES analysis of natural and synthetic basaltic glasses: Implications for S speciation and S content as function of oxygen fugacity. *Geochim. Cosmochim. Acta* 74 (20), 5926–5938.
- Katsura, T., Nagashima, S., 1974. Solubility of sulfur in some magmas at 1 atmosphere. *Geochim. Cosmochim. Acta* 38 (4), 517–531.
- Kelley, K.A., Plank, T., Newman, S., Stolper, E.M., Grove, T.L., Parman, S., Hauri, E.H., 2010. Mantle melting as a function of water content beneath the Mariana Arc. *J. Petrol.* 51 (8), 1711–1738.
- Keppler, H., 1999. Experimental evidence for the source of excess sulfur in explosive volcanic eruptions. *Science* 284 (5420), 1652–1654.
- Kress, V.C., Carmichael, I.S., 1991. The compressibility of silicate liquids containing Fe_2O_3 and the effect of composition, temperature, oxygen fugacity and pressure on their redox states. *Contrib. Mineral. Petrol.* 108 (1), 82–92.
- Lesne, P., Kohn, S.C., Blundy, J., Witham, F., Botcharnikov, R.E., Behrens, H., 2011. Experimental simulation of closed-system degassing in the system basalt– H_2O – CO_2 – S – Cl . *J. Petrol.* 52 (9), 1737–1762.
- Lesne, P., Scaillet, B., Pichavant, M., 2015. The solubility of sulfur in hydrous basaltic melts. *Chem. Geol.* 418, 104–116.
- Li, Y., Feng, L., Kiseeva, E.S., Gao, Z., Guo, H., Du, Z., Wang, F., Shi, L., 2019. An essential role for sulfur in sulfide-silicate melt partitioning of gold and magmatic gold transport at subduction settings. *Earth Planet. Sci. Lett.* 528, 115850.
- Lindgren, W., Ransome, F.L., 1906. *Geology and gold deposits of the Cripple Creek district*, Vol. 54. US Government Printing Office, Colorado.
- Luhr, J.F., 1990. Experimental phase relations of water-and sulfur-saturated arc magmas and the 1982 eruptions of El Chichón volcano. *J. Petrol.* 31 (5), 1071–1114.
- Luhr, J.F., Carmichael, I.S., Varekamp, J.C., 1984. The 1982 eruptions of El Chichón Volcano, Chiapas, Mexico: mineralogy and petrology of the anhydrite-bearing pumices. *J. Volcano Geotherm. Res.* 23 (1–2), 69–108.
- Masotta, M., Keppler, H., 2015. Anhydrite solubility in differentiated arc magmas. *Geochim. Cosmochim. Acta* 158, 79–102.
- Métrich, N., Berry, A.J., O'Neill, H.S.C., Susini, J., 2009. The oxidation state of sulfur in synthetic and natural glasses determined by X-ray absorption spectroscopy. *Geochim. Cosmochim. Acta* 73 (8), 2382–2399.
- Métrich, N., Clochiatti, R., 1996. Sulfur abundance and its speciation in oxidized alkaline melts. *Geochim. Cosmochim. Acta* 60 (21), 4151–4160.
- Moore, G., Vennemann, T., Carmichael, I.S.E., 1998. An empirical model for the solubility of H_2O in magmas to 3 kilobars. *Am. Mineral.* 83 (1–2), 36–42.
- Moretti, R., Ottonello, G., 2005. Solubility and speciation of sulfur in silicate melts: The Conjugated Toop-Samis-Flood-Grjothheim (CTSFG) model. *Geochim. Cosmochim. Acta* 69 (4), 801–823.
- Morizet, Y., Gennaro, E., Jego, S., Zajacz, Z., Iacono-Marziano, G., Pichavant, M., Di Carlo, I., Ferraina, C., Lesne, P., 2017. A Raman calibration for the quantification of SO_4^{2-} groups dissolved in silicate glasses: Application to natural melt inclusions. *Am. Mineral.: J. Earth Planet. Mat.* 102 (10), 2065–2076.
- Moussallam, Y., Oppenheimer, C., Scaillet, B., Gaillard, F., Kyle, P., Peters, N., Hartley, M., Berlo, K., Donovan, A., 2014. Tracking the changing oxidation state of Erebus magmas, from mantle to surface, driven by magma ascent and degassing. *Earth Planet. Sci. Lett.* 393, 200–209.
- Muth, M.J., Wallace, P.J., 2021. Slab-derived sulfate generates oxidized basaltic magmas in the southern Cascade arc (California, USA). *Geology*.
- Namur, O., Charlier, B., Holtz, F., Cartier, C., McCammon, C., 2016. Sulfur solubility in reduced mafic silicate melts: Implications for the speciation and distribution of sulfur on Mercury. *Earth Planet. Sci. Lett.* 448, 102–114.
- Nash, W.M., Smythe, D.J., Wood, B.J., 2019. Compositional and temperature effects on sulfur speciation and solubility in silicate melts. *Earth Planet. Sci. Lett.* 507, 187–198.
- Newman, S., Lowenstern, J.B., 2002. VolatileCalc: a silicate melt– H_2O – CO_2 solution model written in Visual Basic for excel. *Comput. and Geosci.* 28 (5), 597–604.
- Norris, C.A., Wood, B.J., 2017. Earth's volatile contents established by melting and vaporization. *Nature* 549 (7673), 507–510.
- O'Neill, H.S.C., 2005. A method for controlling alkali-metal oxide activities in one-atmosphere experiments and its application to measuring the relative activity coefficients of $\text{NaO}_{0.5}$ in silicate melts. *Am. Mineral.* 90 (2–3), 497–501.
- O'Neill, H.S.C., Mavrogenes, J.A., 2002. The sulfide capacity and the sulfur content at sulfide saturation of silicate melts at 1400 C and 1 bar. *J. Petrol.* 43 (6), 1049–1087.
- O'Neill, H.S.C., Mavrogenes, J.A., 2022. The sulfate capacities of silicate melts. *Geochim. Cosmochim. Acta*.
- Osborn, E.F., Tait, D.B., 1952. The system diopside-forsterite-anorthite. *Am. J. Sci.* 250, 413–433.
- Parat, F., Holtz, F., Streck, M.J., 2011. Sulfur-bearing magmatic accessory minerals. *Rev. Mineral. Geochem.* 73 (1), 285–314.
- Prausnitz, J.M., Lichtenthaler, R.N., De Azevedo, E.G., 1999. *Molecular thermodynamics of fluid-phase equilibria*. Prentice Hall, New Jersey.
- Presnall, D.C., Dixon, S.A., Dixon, J.R., O'donnell, T.H., Brenner, N.L., Schrock, R.L., Dycus, D.W., 1978. Liquidus phase relations on the join diopside-forsterite-anorthite from 1 atm to 20 kbar: their bearing on the generation and crystallization of basaltic magma. *Contrib. Mineral. Petrol.* 66 (2), 203–220.
- Ridley, W.I., 1970. The petrology of the Las Canadas volcanoes, Tenerife, Canary Islands. *Contrib. Mineral. Petrol.* 26 (2), 124–160.
- Robie, R.A., Hemingway, B.S., Fisher, J.R., 1978. *Thermodynamic properties of minerals and related substances at 298.15 K and 1 bar (105 pascals) pressure and at higher temperatures*.
- Simon, A.C., Ripley, E.M., 2011. The role of magmatic sulfur in the formation of ore deposits. *Rev. Mineral. Geochem.* 73 (1), 513–578.
- Sossi, P.A., Klemme, S., O'Neill, H.S.C., Berndt, J., Moynier, F., 2019. Evaporation of moderately volatile elements from silicate melts: experiments and theory. *Geochim. Cosmochim. Acta* 260, 204–231.
- Sugawara, T., 1999. Experimental techniques to minimize Fe and Na losses in one atmosphere gas mixing furnace. *J. Mineral. Petrol. Eco. Geol.* 94 (11), 425–441.
- Taracsák, Z., Neave, D.A., Beaudry, P., Gunnarsson-Robin, J., Burgess, R., Edmonds, M., Halldórsson, S.A., Longpré, M.-A., Ono, S., Ranta, E., Stefánsson, A., Turchyn, A.V., EIMF, Hartley, M.E., 2021. Instrumental mass fractionation during sulfur isotope analysis by secondary ion mass spectrometry in natural and synthetic glasses. *Chem. Geol.* 578, 120318.
- Thomas, R.W., Wood, B.J., 2021. The chemical behaviour of chlorine in silicate melts. *Geochim. Cosmochim. Acta* 294, 28–42.
- Tsujimura, T., Kitakaze, A., 2005. Experimental study of sulfur solubility in silicate melts coexisting with graphite as a function of silicate melt composition. *Resour. Geol.* 55 (1), 55–60.
- Verhooijen, J., 1949. Thermodynamics of a magmatic gas phase 28, 91–136.
- Wallace, P.J., Carmichael, I.S., 1994. S speciation in submarine basaltic glasses as determined by measurements of S K α X-ray wavelength shifts. *Am. Mineral.* 79 (1–2), 161–167.
- Webb, S.L., Dingwell, D.B., 1990. Non-Newtonian rheology of igneous melts at high stresses and strain rates: Experimental results for rhyolite, andesite, basalt, and nephelinite. *J. Geophys. Res.: Solid Earth* 95 (B10), 15695–15701.
- Webster, J.D., Botcharnikov, R.E., 2011. Distribution of sulfur between melt and fluid in SOHC-Cl -bearing magmatic systems at shallow crustal pressures and temperatures. *Rev. Mineral. Geochem.* 73 (1), 247–283.
- White, W.B., Johnson, S.M., Dantzig, G.B., 1958. Chemical equilibrium in complex mixtures. *J. Chem. Phys.* 28 (5), 751–755.
- Wilke, M., Jugo, P.J., Klimm, K., Susini, J., Botcharnikov, R., Kohn, S.C., Janousch, M., 2008. The origin of S^{4+} detected in silicate glasses by XANES. *Am. Mineral.* 93 (1), 235–240.
- Wood, B.J., Turner, S.P., 2009. Origin of primitive high-Mg andesite: Constraints from natural examples and experiments. *Earth Planet. Sci. Lett.* 283 (1–4), 59–66.
- Xu, Z., Li, Y., 2021. The sulfur concentration at anhydrite saturation in silicate melts: Implications for sulfur cycle and oxidation state in subduction zones. *Geochim. Cosmochim. Acta* 306, 98–123.
- Zajacz, Z., Candela, P.A., Piccoli, P.M., Sanchez-Valle, C., 2012. The partitioning of sulfur and chlorine between andesite melts and magmatic volatiles and the exchange coefficients of major cations. *Geochim. Cosmochim. Acta* 89, 81–101.
- Zajacz, Z., Tsay, A., 2019. An accurate model to predict sulfur concentration at anhydrite saturation in silicate melts. *Geochim. Cosmochim. Acta* 261, 288–304.
- Zimmer, M.M., Plank, T., Hauri, E.H., Yogodzinski, G.M., Stelling, P., Larsen, J., Singer, B., Jicha, B., Mandeville, C., Nye, C.J., 2010. The role of water in generating the calc-alkaline trend: new volatile data for Aleutian magmas and a new tholeiitic index. *J. Petrol.* 51 (12), 2411–2444.